Available online at www.sciencedirect.com
ScienceDirect
Geochimica et Cosmochimica Acta 72 (2008) 3258–3286
Geochimica et Cosmochimica Acta
www.elsevier.com/locate/gca

Between carbonatite and lamproite—Diamondiferous Torngat ultramafic lamprophyres formed by carbonate-fluxed melting of cratonic MARID-type metasomes

Sebastian Tappe [a,*], Stephen F. Foley [b], Bruce A. Kjarsgaard [c], Rolf L. Romer [d], Larry M. Heaman [a], Andreas Stracke [e], George A. Jenner [f]

[a] De Beers Canada Inc., 65, Overlea Boulevard, Suite 300, Toronto, Ont., Canada M4H 1P1
[b] Institut für Geowissenschaften, Universität Mainz, Becherweg 21, 55099 Mainz, Germany
[c] Geological Survey of Canada, Ottawa, Canada K1A 0E8
[d] GeoForschungszentrum Potsdam, Telegrafenberg, 14473 Potsdam, Germany
[e] Institut für Isotopengeologie und Mineralische Rohstoffe, Department of Earth Sciences, ETH-Zürich, Clausiusstrasse 25, CH-8092 Zürich, Switzerland
[f] Department of Earth Sciences, Memorial University, St. John's, Canada A1B 3X5

Received 12 November 2007; accepted in revised form 11 March 2008; available online 30 March 2008

Abstract

New U–Pb perovskite ages reveal that diamondiferous ultramafic lamprophyre magmas erupted through the Archean crust of northern Labrador and Quebec (eastern Canada) between ca. 610 and 565 Ma, a period of strong rifting activity throughout contiguous Laurentia and Baltica. The observed Torngat carbonate-rich aillikite/carbonatite and carbonate-poor mela-aillikite dyke varieties show a large spread in Sr–Nd–Hf–Pb isotope ratios with pronounced correlations between isotope systems. An isotopically depleted component is identified solely within aillikites ($^{87}Sr/^{86}Sr_i = 0.70323–0.70377$; $\varepsilon Nd_i = +1.2–+1.8$; $\varepsilon Hf_i = +1.4–+3.5$; $^{206}Pb/^{204}Pb_i = 18.2–18.5$), whereas some aillikites and all mela-aillikites range to more enriched isotope signatures ($^{87}Sr/^{86}Sr_i = 0.70388–0.70523$; $\varepsilon Nd_i = -0.5$ to -3.9; $\varepsilon Hf_i = -0.6$ to -6.0; $^{206}Pb/^{204}Pb_i = 17.8–18.2$). These contrasting isotopic characteristics of aillikites/carbonatites and mela-aillikites, along with subtle differences in their modal carbonate, SiO_2, Al_2O_3, Na_2O, Cs–Rb, and Zr–Hf contents, are consistent with two distinctive metasomatic assemblages of different age in the mantle magma source region.

Integration of petrologic, geochemical, and isotopic information leads us to propose that the isotopically enriched component originated from a reduced phlogopite-richterite-Ti-oxide dominated source assemblage that is reminiscent of MARID suite xenoliths. In contrast, the isotopically depleted component was derived from a more oxidized phlogopite-carbonate dominated source assemblage. We argue that low-degree CO_2-rich potassic silicate melts from the convective upper mantle were preferentially channelled into an older, pre-existing MARID-type vein network at the base of the North Atlantic craton lithosphere, where they froze to form new phlogopite-carbonate dominated veins. Continued stretching and thinning of the cratonic lithosphere during the Late Neoproterozoic remobilized the carbonate-rich vein material and induced volatile-fluxed fusion of the MARID-type veins and the cold peridotite substrate. Isotopic modelling suggests that only 5–12% trace element contribution from such geochemically extreme MARID-type material is required to produce the observed compositional shift from the isotopically most depleted aillikites/carbonatites towards enriched mela-aillikites.

We conclude that cold cratonic mantle lithosphere can host several generations of contrasting vein assemblages, and that each may have formed during past tectonic and magmatic events under distinctively different physicochemical conditions. Although cratonic MARID-type and carbonate-bearing veins in peridotite can be the respective sources for lamproite and

* Corresponding author. Fax: +1 416 423-9919.
E-mail address: sebastian.tappe@ca.debeersgroup.com (S. Tappe).

0016-7037/$ - see front matter © 2008 Published by Elsevier Ltd.
doi:10.1016/j.gca.2008.03.008

carbonatite magmas when present as the sole metasome, their concomitant fusion in a complex source region may give rise to a whole new variety of deep volatile-rich magmas and we suggest that orangeites (formerly Group 2 kimberlites), kamafugites, and certain types of ultramafic lamprophyre are formed in this manner.

1. INTRODUCTION

Carbonatites and lamproites are some of the most extreme partial melting products of mantle materials that have been previously enriched in incompatible elements and volatiles. On the basis of experimental studies they appear to represent opposite ends of the volatile spectrum; carbonatites clearly require abundant CO_2 in the source (Wyllie and Huang, 1975; Olafsson and Eggler, 1983; Eggler, 1989; Wyllie, 1989), whereas lamproites require H_2O-rich sources (Arima and Edgar, 1983b; Foley et al., 1987; Edgar and Vukadinovic, 1992) in which carbon, if present in any abundance at all, probably exists as CH_4 (Foley et al., 1986; Foley, 1993). Coupled to these distinctive volatile compositions in the source regions, carbonatites and lamproites each have highly specific characteristics as regards major element composition and incompatible element distribution, indicating contrasting source enrichment styles that resulted in specific metasomatic assemblages (Green and Wallace, 1988; Meen et al., 1989; Foley, 1992a,b; Thibault et al., 1992; Mitchell, 1995; Chakhmouradian, 2006). In this paper we present the case for the concurrent melting of two such contrasting metasomatic assemblages that had been introduced into the North Atlantic craton (NAC) mantle lithosphere at different times. The outcome was a suite of carbonate-potassic silicate magmas, the *Torngat ultramafic lamprophyres*, which form a diamondiferous dyke swarm across northern Labrador and easternmost Quebec, Canada (Tappe et al., 2004).

The Torngat ultramafic lamprophyre (UML) suite comprises rare dolomite carbonatite and abundant aillikite, which is the carbonate-rich UML variant. Aillikite compositionally grades into carbonate-poor (to carbonate-free) varieties, for which we introduced the term mela-aillikite (Tappe et al., 2004, 2005). Although we previously noted these mela-aillikites can have mineralogical similarities to olivine lamproites, i.e., the occurrence of olivine and phlogopite phenocrysts with groundmass high-Ti potassian richterite, they differ from olivine lamproites in being significantly SiO_2-undersaturated (30–37 wt% as opposed to 41–46 wt% SiO_2 for typical olivine lamproites; Mitchell and Bergman, 1991; Foley, 1993). This points to aillikite and, importantly, mela-aillikite magma generation in the presence of CO_2 (cf. Green and Falloon, 1998), a volatile species not essential in the genesis of lamproites (Foley et al., 1986). Previously, CO_2 degassing during UML magma emplacement was suggested as a possible explanation for the Torngat aillikite/carbonatite and mela-aillikite compositional continuum (Tappe et al., 2004).

In this study we report U–Pb perovskite ages, radiogenic (Sr–Nd–Hf–Pb) and stable (C–O) isotope compositions of the Torngat UML suite complemented by data from newly discovered UML dykes from the northern Labrador coast (Fig. 1). We argue that the UML magmas formed by melting of a young phlogopite-carbonate dominated vein assemblage, which caused carbonate-fluxed fusion of ancient cratonic MARID-type veins and the peridotite substrate. If this mechanism gave rise to the aillikite/carbonatite and mela-aillikite continuum described here, then it appears that the Torngat case straddles conceptual borderlines between carbonatite and lamproite magma geneses. It may thus provide an alternative perspective on the origin of deep volatile-rich magmas (e.g., orangeites and kamafugites) and the processes that surround alkaline melt production at high pressures.

2. BACKGROUND

2.1. North Atlantic craton, Torngat Mountains, and diamondiferous UML dykes

Two contrasting Archean domains are juxtaposed in northern Labrador (Fig. 1). The Early Archean Saglek block to the east shares many compositional and structural features with the tonalitic crust of western Greenland and, thus, was assigned to the North Atlantic craton (Bridgwater et al., 1973). The reworked Late Archean block to the west is poorly understood and has been variably assigned to the Churchill (Rae subdomain) or the Superior provinces (Korstgård et al., 1987; Rivers et al., 1996; Wardle et al., 2002). Less uncertain, however, is that these two ancient terranes collided at about 1900 to 1800 Ma (Hoffman, 1990), from then on forming an integral part of the supercraton Laurentia (Hoffman, 1988). The Paleoproterozoic suture zones form high-grade orogenic belts with steep topography, for example the Torngat Mountains of northern Labrador and Quebec (Rivers et al., 1996).

Numerous UML dykes occur in northern Labrador and Quebec following a northwest to northeast trend (300° to 060°). They are undeformed, up to 3-m-wide, steeply dipping (>45°), and individual segments can be traced for several kilometres along strike. Digonnet et al. (2000) reported a $^{40}Ar/^{39}Ar$ phlogopite age of 550 ± 15 Ma (2σ) for an aillikite dyke from Abloviak Fjord in the Torngat Mountains of northern Quebec. Tappe et al. (2004) demonstrated the extension of this UML swarm into Labrador to the southeast and emphasized the compositional diversity. The aillikite/carbonatite and mela-aillikite dyke varieties recognized in the Abloviak Fjord region were collectively referred to as 'Torngat UML' by Tappe et al. (2004), who determined an U–Pb perovskite emplacement age of 584.0 ± 3.6 Ma (2σ) for aillikite dyke Q39. These dykes intruded an area that is at least 1500 km^2 in size and, thus, form one of the largest known UML swarms. Some of the Torngat UMLs contain sparse but high-quality diamonds (up to 0.685 carats; Twin

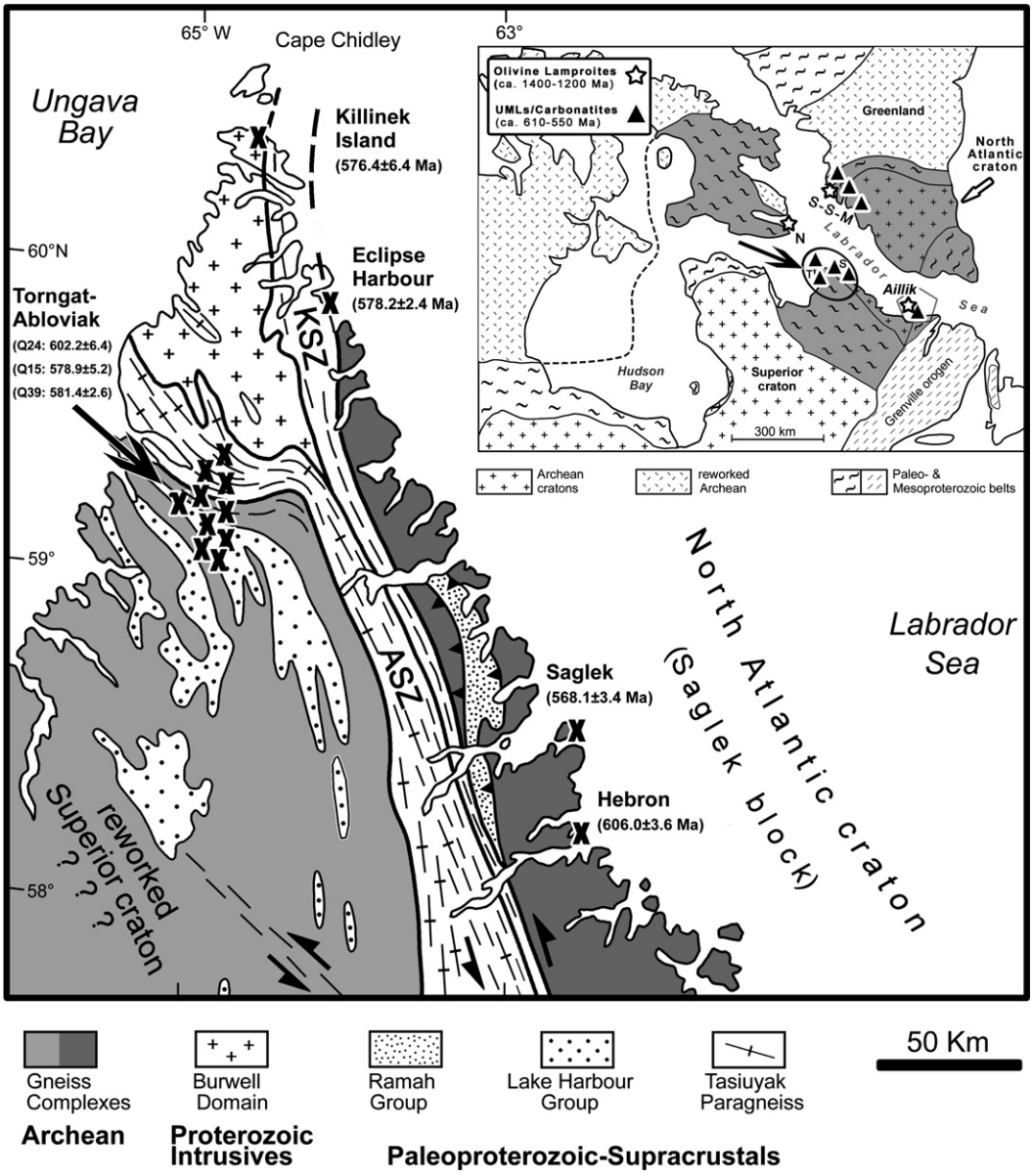

Fig. 1. Simplified geological map of the Torngat Mountains in northern Labrador and Quebec (modified from Wardle et al., 2002). The Torngat and Saglek block UML dyke occurrences investigated during this study are shown as black Xs. The new U–Pb perovskite ages and 2σ errors are given in brackets. The inset map provides an overview of the northeastern Canadian–Greenland Shield with grey-shaded areas representing the North Atlantic craton with surrounding mobile belts on either side of the Labrador Sea. Mesoproterozoic olivine lamproite (ca. 1400 to 1200 Ma) and Neoproterozoic UML/carbonatite (ca. 610 to 550 Ma) occurrences in the vicinity of the Labrador Sea are also shown. Note that the position of Greenland is restored for Cenozoic continental drift due to now extinct sea-floor spreading in the Labrador Sea (modified from Tappe et al., 2007). Tectonic features and alkaline rock occurrences mentioned in the text are abbreviated as follows: ASZ, Abloviak shear zone; KSZ, Komaktorvik shear zone; N, Napoleon Bay; S, Saglek block; SSM, Sisimiut–Sarfartoq–Maniitsoq areas; T, Torngat Mountains.

Mining Annual Report 2002; http://www.sedar.com). The Torngat samples provide the basis for this isotope study and we have included new UML samples from the northern Labrador coast at Hebron, Saglek, Eclipse Harbour, and Killinek Island in order to examine potential variations among UMLs from different cratonic entities. These four coastal Labrador samples are hereafter collectively referred to as the 'Saglek block UML' (Fig. 1).

2.2. Aillikite/carbonatite and mela-aillikite compositional continuum

Aillikite is the carbonate-rich member of the UML group (Rock, 1991; Tappe et al., 2005), which encompasses olivine- and phlogopite-bearing hypabyssal rocks (Fig. 2) derived from a volatile-rich, potassic, SiO_2-poor parental magma. In general, aillikite dykes are often found in the

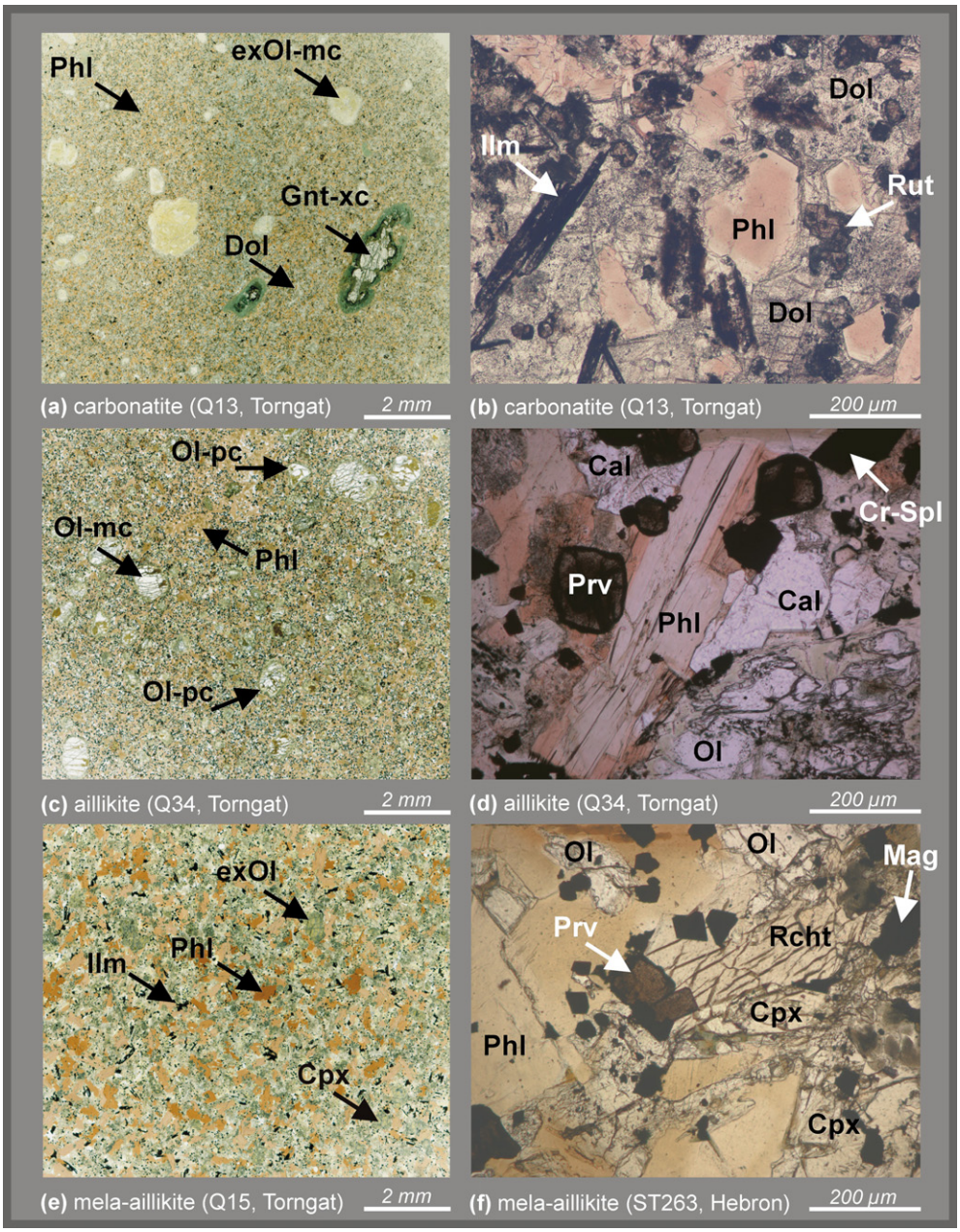

Fig. 2. Overview thin section scans (left) and photomicrographs (plane polarized light, right) of the northern Labrador aillikite/carbonatite and mela-aillikite dyke rocks: (a) Fine-grained dolomite carbonatite Q13 containing few olivine macrocrysts (Ol-mc) and pyrope garnet xenocrysts (Gnt-xc) set in a dolomite and phlogopite dominated matrix. (b) Photomicrograph of dolomite carbonatite Q13 showing the dolomite (Dol) and phlogopite (Phl) dominated matrix plus rutile (Rut) grains and ilmenite (Ilm) laths. (c) Porphyritic aillikite Q34 containing abundant olivine (Ol-pc) and phlogopite phenocrysts, as well as rare olivine macrocrysts set in a carbonate groundmass.(d) Photomicrograph of aillikite Q34 showing olivine, phlogopite, chromian spinel (Cr-Spl), and perovskite (Prv) microphenocrysts in a calcite (Cal) groundmass. (e) Intergranular mela-aillikite Q15 with abundant phlogopite plates, clinopyroxene (Cpx) prisms, and ilmenite laths. Rare carbonate is restricted to the interstices between mafic silicate crystals. (f) Photomicrograph of Hebron mela-aillikite ST263 exhibiting diopside-rich clinopyroxene and titanian magnesiokatophorite-rich richteritic amphibole prisms (Rcht) that are confined to interstitial space between large phlogopite plates. Note furthermore the fresh olivine, magnetite (Mag), and perovskite microphenocrysts that are typically enclosed by phlogopite plates.

vicinity of carbonatite intrusions and can be observed grading into varieties of carbonatite where they have >50 vol % modal carbonate. Recently, Mitchell (2005) suggested a lower limit of 30 vol % carbonate in order to reinforce the genetic link between, for example, some aillikites and carbonatites. Prime examples of this association are observed at Fen in Scandinavia (e.g., Dahlgren, 1994), Sarfartoq in western Greenland (e.g., Larsen and Rex, 1992; Mitchell et al., 1999), and Aillik Bay in central Labrador (e.g., Tappe et al., 2006). However, regional aillikite dyke swarms also

occur in areas where there is no indication of central-complex carbonatite intrusions, such as in the Torngat Mountains. In this area, Late Neoproterozoic aillikite/carbonatite and carbonate-poor mela-aillikite dykes co-exist, and appear to represent a compositional continuum between carbonate-rich and carbonate-free end-members. The following provides background information about the Torngat UMLs summarized from Tappe et al. (2004).

The Torngat mela-aillikites contain significant groundmass clinopyroxene and rare richteritic amphibole instead of abundant primary carbonate (Fig. 2). This reflects lower CO_2 (<5 wt%), but slightly elevated SiO_2 (30–37.4 wt%), Al_2O_3 (4–6 wt%), and Na_2O (0.3–0.9 wt%) contents compared to the aillikite magma (3-22 wt% CO_2; 22–30 wt% SiO_2; 2.2–4.4 wt% Al_2O_3; <0.3 wt% Na_2O; Fig. 3). However, Torngat aillikites and mela-aillikites have overlapping high MgO (12–24 wt%), Ni (229–1110 ppm), and Cr (290–1570 ppm) contents and, thus, cannot be related by fractional crystallization of spinels and/or common mafic silicate minerals such as olivine. Furthermore, overlapping high TiO_2 (3–10 wt%) and K_2O (1.4–3.5 wt%; Fig. 3) excludes a genetic link between the UML varieties by fractionation or accumulation of Ti-oxides and/or phlogopite. Some aillikites are conspicuously richer in ferric iron than mela-aillikites (0.4–2.3 vs. 0.7–1.7 Fe_2O_3/FeO) at similar bulk-rock total iron contents, implying these magmas record different primary oxidation states (Tappe et al., 2004).

Based on their mineral assemblages and compositions, Tappe et al. (2004) interpreted the Torngat aillikites and mela-aillikites as being derived from a common magma but following different crystallization paths due to CO_2 loss, distinctive cooling histories, and variable redox conditions during emplacement. Here, we utilize tracer isotope ratios that allow us to formulate a more robust model in which the aillikite/carbonatite and mela-aillikite compositional continuum is related to the melting process of a common but heterogeneous upper mantle source region.

3. ANALYTICAL TECHNIQUES

3.1. U–Pb perovskite geochronology

Two aillikite and five mela-aillikite hand specimens were processed through standard crushing and mineral separation procedures (Wilfley table, methylene iodide, Frantz isodynamic separator) at the University of Alberta following the techniques described in Heaman and Kjarsgaard (2000). Perovskite recovery was best in 20–100 μm range. Fresh euhedral crystals without visible inclusions were individually selected, collected as morphologic fractions and dissolved in a mixture of HF and HNO_3 (typically more than 100 grains per fraction to obtain >50 μg aliquots). A ^{235}U–^{205}Pb tracer was added to the perovskite/acid mix before dissolution in order to determine U and Pb concentrations by isotope dilution. Thorium concentrations were calculated based on the amount of ^{208}Pb present and the $^{207}Pb/^{206}Pb$ model age. Uranium and Pb were isolated and concentrated from perovskite using a HBr anion exchange chromatography technique. The isotopic composition of these elements was measured on a VG354 thermal ionization mass spectrometer operating in analogue Daly mode. All isotopic data reported in Table 1 were corrected for mass discrimination (0.105%/amu Pb and 0.123%/amu U), tracer, and blank contribution. The presence of initial common lead was corrected using the terrestrial lead evolution model of Stacey and Kramers (1975). The $^{206}Pb/^{238}U$ perovskite ages were shown to be most robust because they are least sensitive to this initial common lead correction (Heaman, 1989; Heaman and Kjarsgaard, 2000).

3.2. Bulk-rock major and trace element composition

Rock powders of <20 μm grain size were prepared in an agate planetary ball mill at the Universities of Greifswald and Mainz (Germany) and supplied to Activation Laboratories (Ancaster, Canada) for analyses. Major elements and selected trace elements were determined using a fusion digestion and ICP-AES; and representative analyses have already been published in Tappe et al. (2004). Some samples were additionally analyzed by XRF on fused glass discs at the Universities of Greifswald and Mainz. Results of the two techniques agree within analytical uncertainty. Rare earth elements and other trace elements (e.g., Nb, Th, U) were analysed using an acid dissolution and ICP-MS. The U and Pb concentrations of those samples analyzed for Pb isotope composition were determined by ID-TIMS in Potsdam (Germany) using a mixed ^{235}U-^{208}Pb tracer. Concentrations for elements determined by ICP-MS and XRF (e.g., Sr, Ce, Y, Zr, U, Th, and Pb), as well as ID-TIMS (U and Pb) compare within analytical error. Volatiles were determined by a combination of loss on ignition (corrected for the conversion of FeO to Fe_2O_3) and direct determination of CO_2 using a C–S analyser.

3.3. Bulk-rock Sr–Nd–Hf–Pb isotope composition

Isotope compositions were determined on the same bulk-rock powders as the major and trace element contents. Two sample dissolution setups were tested: (1) Powders were loaded together with HF/HNO_3 in microcapsules, which were placed together in an external Teflon-lined steel autoclave, and heated in an oven at 160 °C for 7 days. (2) Powders were attacked in a HF/HNO_3 mixture in Savillex beakers on a hotplate for 3 days. Subsequently, the HF/HNO_3 mixture from both acid digestion procedures was gently evaporated to incipient sample dryness. The sample material was then taken up in 6 N HCl and heated again until a clear solution was obtained; i.e., for 2–3 days. This test indicated complete sample dissolution without bombs, because the measured Hf isotope composition of duplicate pairs of aillikite Q24 and mela-aillikite Q23 are identical within analytical error (Electronic Annex A). Thus, the less tedious powder digestion procedure using Savillex beakers was applied for the remainder of the samples.

Sr and Nd were separated and concentrated by standard procedures using Bio-Rad AG50W cation and Eichrom Ln-Spec anion exchange resin, respectively. Sr and Nd isotope compositions were measured on a VG 54-30 Sector (Ta single filaments) and Finnigan MAT 262 (Re double filaments) thermal ionization mass spectrometer, respectively, in dynamic mode (GFZ Potsdam, Germany). The measured $^{87}Sr/^{86}Sr$ ratios were normalized to $^{86}Sr/^{88}Sr = 0.1194$ and $^{143}Nd/^{144}Nd$ to $^{146}Nd/^{144}Nd = 0.7219$. During the measurement period, the NBS-987 Sr reference material yielded an average value for $^{87}Sr/^{86}Sr$ of 0.710270 ± 14 (2σ SD for 18 measurements) and the La Jolla standard yielded a $^{143}Nd/^{144}Nd$ value of 0.511850 ± 7 (2σ S.D. for 11 measurements).

Hf was separated using Eichrom Ln-Spec anion exchange resin following the procedure described by Münker et al. (2001). The Hf isotopic composition was analyzed by plasma ionization multi-collector mass spectrometry (MC-ICP-MS) on a *Nu* Plasma multi-collector ICP-MS instrument in static mode (MPI Mainz, Germany) and all isotope ratios were corrected with an exponential fractionation law using $^{179}Hf/^{177}Hf = 0.7325$. Mass ^{173}Yb and ^{175}Lu were monitored for isobaric interferences of ^{176}Yb and ^{176}Lu

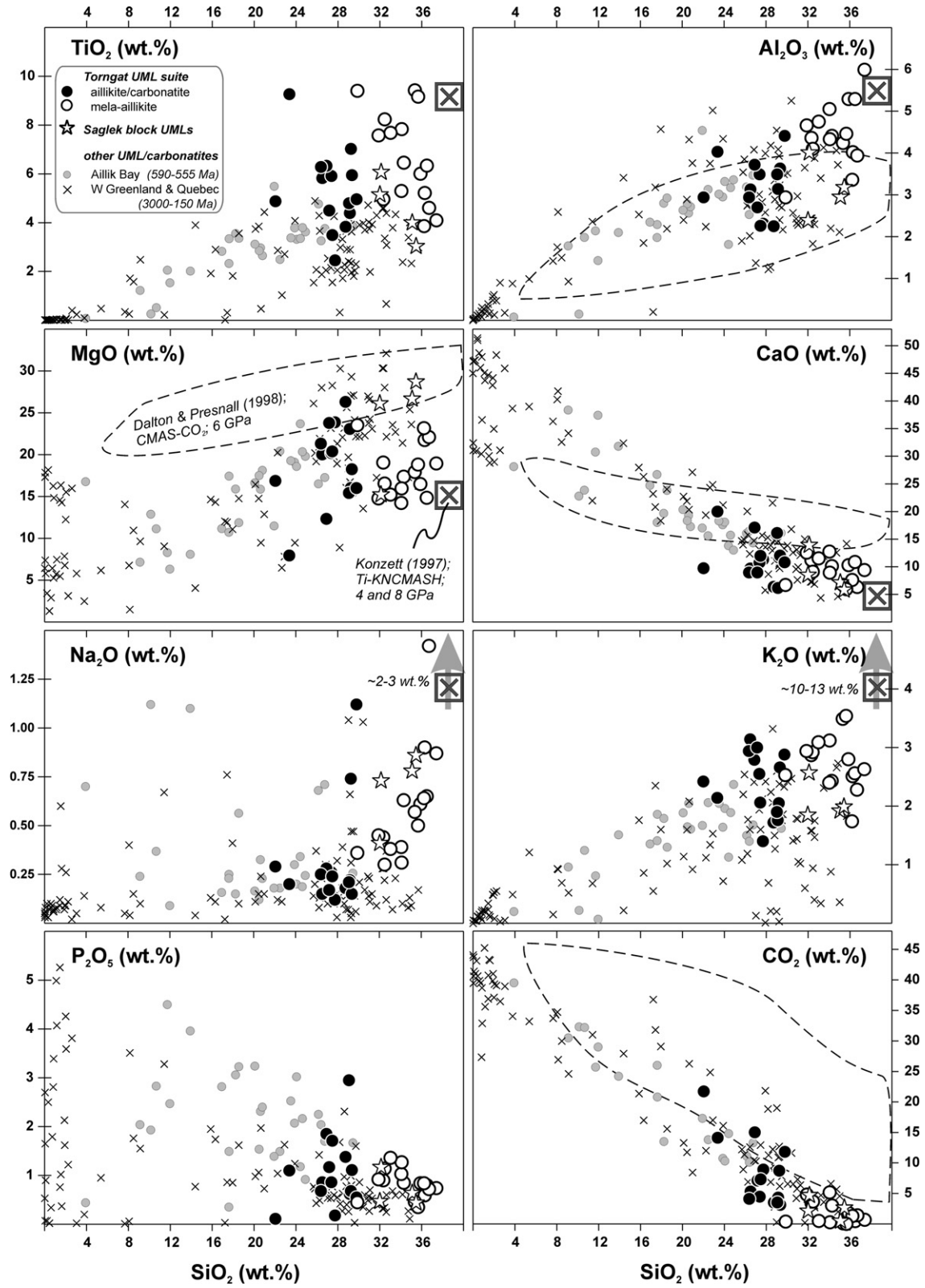

Fig. 3. Major element oxide vs. SiO_2 (wt%) for the Torngat and Saglek block aillikite/carbonatite and mela-aillikite dykes. The dashed field shows the compositional range of six near-solidus melts including 1σ errors produced experimentally from synthetic carbonated peridotite in a simple CMAS–CO_2 system at 6 GPa (Dalton and Presnall, 1998). The grey box with the cross shows the area covered by two experimental melt compositions produced from a synthetic MARID-type starting material in a Ti–KNCMASH system at 4 and 8 GPa (Konzett, 1997). Other UML/carbonatite intrusives from central Labrador (Aillik Bay), western Greenland, and eastern Quebec of various ages belonging to the aillikite—carbonatite association are shown for comparison. Data sources are available from the first author upon request.

Table 1
U–Pb perovskite results for ultramafic lamprophyre dykes from the Torngat Mountains and the Saglek block, North Atlantic craton, Labrador, Canada

Description[a]	Weight (μg)	U (ppm)	Th (ppm)	Pb (ppm)	Th/U	TCPb (pg)	$^{206}Pb/^{238}U$[b]	$^{207}Pb/^{235}U$[b]	$^{207}Pb/^{206}Pb$[b]	Apparent ages (Ma)			
										$^{206}Pb/^{238}U$	$^{207}Pb/^{235}U$	$^{207}Pb/^{206}Pb$	Discordance [%]
Torngat Q39 (aillikite)													
1. Dark brown fragments/cubes; M@0.5 A (100)	38	105	587	29	5.6	187	0.09483 ± 30	0.7976 ± 93	0.06101 ± 68	**584.0 ± 1.8**	595.5 ± 5.3	639 ± 24	9.1
2. Dark brown fragments/cubes; M@0.5 A (246)	50	130	729	36	5.6	296	0.09388 ± 32	0.7818 ± 97	0.06040 ± 74	**578.5 ± 1.9**	586.5 ± 5.6	618 ± 26	6.7
Torngat Q24 (aillikite)													
Brown clear cubes/octahedrons; M@0.5 A (100)	105	55	415	25	7.6	1140	0.09792 ± 55	0.7835 ± 345	0.05803 ± 258	**602.2 ± 3.2**	588 ± 20	531 ± 95	−14
Torngat Q15 (mela-aillikite)													
Black irregular fragments; MI@H (40)	225	127	1655	58	13	1020	0.09395 ± 43	0.7739 ± 715	0.05974 ± 51	**578.9 ± 2.6**	582.0 ± 4.1	594 ± 19	2.7
Hebron ST263 (mela-aillikite)													
Dark brown irregular fragments; M@0.5 A (152)	293	133	150	22	1.1	1850	0.09857 ± 30	0.8064 ± 977	0.05933 ± 70	**606.0 ± 1.8**	600.4 ± 5.5	579 ± 25	−4.8
Saglek ST264 (mela-aillikite)													
Black irregular fragments; M@0.3A (150)	22	44	1222	33	28	68	0.09212 ± 29	0.7213 ± 228	0.05679 ± 172	**568.1 ± 1.7**	551 ± 13	483 ± 65	−18
Killinek Island ST266 (mela-aillikite)													
Brown clear octahedrons/fragments; MI@H (80)	80	52	509	22	9.7	371	0.09353 ± 54	0.7767 ± 162	0.06023 ± 129	**576.4 ± 3.2**	583.6 ± 9.2	612 ± 46	6.0
Eclipse Harbour ST267 (mela-aillikite)													
Black irregular fragments; M@0.4A (150)	63	170	667	35	3.9	171	0.09383 ± 20	0.7673 ± 438	0.05930 ± 31	**578.2 ± 1.2**	578.2 ± 2.5	578 ± 11	0.0

Thorium concentrations calculated based on amount of ^{208}Pb present and $^{207}Pb/^{206}Pb$ model age. TCPb is estimated total initial common Pb based on the Stacey and Kramers (1975) Pb evolution model. U–Pb data for 'perovskite fraction 1' of aillikite Q39 are from Tappe et al. (2004). All errors reported in this table are quoted at 1σ.

[a] M@0.5 A—perovskite grains selected from non-magnetic fraction at 0.5 A (Frantz); MI@H—perovskite grains selected from heavy fraction after methylene iodide separation; numbers in parentheses are numbers of grains analysed.

[b] Atomic ratios corrected for fractionation, blank (1 pg Pb; 0.5 pg U), isotopic tracer, and initial common Pb.

on mass ^{176}Hf. ^{176}Lu interferences were negligible and the contribution of ^{176}Yb to the ^{176}Hf signal never exceeded 0.005% during analysis. The JMC-475 Hf standard was run repeatedly during each analytical session with a mean average for $^{176}Hf/^{177}Hf$ of 0.282168 ± 17 (2σ SD for 48 measurements) during the measurement period. This is in good agreement with the long-term average of 0.282161 ± 16 (2σ SD for 415 measurements).

Pb from rock powders was separated using anion exchange resin Bio-Rad AG1-X8 applying the HCl-HBr technique described by Romer et al. (2005). The Pb isotopic composition was measured on a Finnigan MAT 262 instrument on single Re filaments in static mode (GFZ Potsdam, Germany). Instrumental fractionation was corrected with +0.1% per amu as determined from the long-term reproducibility of Pb reference material NBS-981. Accuracy and precision of reported Pb isotope ratios is better than 0.1% at the 2σ level of uncertainty.

Total procedural blanks are less than 50 pg Sr, 30 pg Nd, 200 pg Hf, 30 pg Pb, and considered negligible given the high concentrations of these elements in the samples analysed. The initial Sr, Nd, Hf, and Pb isotopic compositions of the UML dykes were calculated for an intrusion age of 582 Ma (Torngat Mountains), 606 Ma (Hebron), 568 Ma (Saglek), 578 Ma (Eclipse Harbour), and 576 Ma (Killinek Island) using the following decay constants: ^{87}Rb 1.42×10^{-11} a^{-1} (Steiger and Jäger, 1977); ^{147}Sm 6.54×10^{-12} a^{-1} (Lugmair and Marti, 1978); ^{176}Lu 1.865×10^{-11} a^{-1} (Scherer et al., 2001); ^{232}Th 4.9475×10^{-11} a^{-1}; ^{235}U 9.8485×10^{-10} a^{-1}; ^{238}U 1.55125×10^{-10} a^{-1} (Jaffey et al., 1971; Steiger and Jäger, 1977).

3.4. Carbon and oxygen isotope composition

The carbon and oxygen isotope composition of bulk-rock carbonate fractions was measured at the University of Alberta, Canada. Rock powders were reacted with anhydrous H_3PO_4 under vacuum at 25 °C for ca. 24 h in order to liberate CO_2. CO_2 gas recoveries were close to 100% of theoretical yields so no isotope fractionation during dissolution should have occurred. We applied acid fractionation factors of 1.01025 and 1.01178 to calcite- and dolomite-bearing samples, respectively. The purified CO_2 was analysed using a Finnigan MAT-252 gas source mass spectrometer and measured isotope ratios are expressed as δ^{13}C and δ^{18}O‰ relative to PDB (Pee Dee Belemnite) and SMOW (Standard Mean Ocean Water), respectively. Reproducibility was better than 0.1‰ for δ^{13}C and 0.2‰ for δ^{18}O as determined by repeated measurements ($n = 9$, 2σ SD) of an in-house limestone standard.

4. NEW U–PB PEROVSKITE AGES

U–Pb perovskite ages were determined for seven individual UML dykes from the Torngat Mountains and the Saglek block along the western NAC edge (Fig. 1). Data are reported in Table 1 and illustrated in Fig. 4. In general, the uranium contents (44–170 ppm) and Th/U ratios (1.1–13.1) of perovskite isolated from these UML dykes are similar to perovskite from North American kimberlites (Heaman and Kjarsgaard, 2000). However, perovskite from the Saglek mela-aillikite ST264 has a higher than average Th/U ratio of 27.5.

A second perovskite fraction from the previously dated Torngat aillikite dyke Q39 (Tappe et al., 2004) was analyzed during this study and yielded a $^{206}Pb/^{238}U$ age of 578.5 ± 3.8 Ma, which is similar to the published age of 584.0 ± 3.6 Ma (errors are quoted at the 2σ level of uncertainty throughout the text). Hence, a weighted average $^{206}Pb/^{238}U$ age of 581.4 ± 2.6 Ma is considered the best estimate for emplacement of this aillikite dyke. Perovskite from Torngat mela-aillikite dyke Q15 yielded a similar $^{206}Pb/^{238}U$ age of 578.9 ± 5.2 Ma. The age of Torngat aillikite dyke Q24 is slightly older at 602.2 ± 6.4 Ma and represents the oldest emplacement age yet determined from the Torngat UML dyke swarm. If only these U–Pb age determinations are taken into account, then the Torngat aillik-

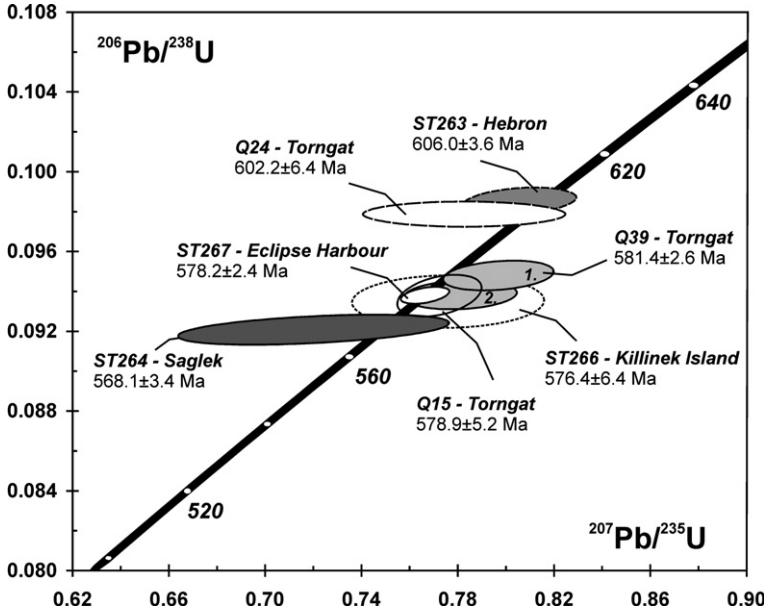

Fig. 4. U–Pb perovskite results for aillikite and mela-aillikite dykes from the Torngat Mountains and the Saglek block in northern Labrador displayed in a concordia diagram. Reported ages are $^{206}Pb/^{238}U$ dates with quoted uncertainties and envelopes at 2σ. For Torngat aillikite Q39 a weighted average $^{206}Pb/^{238}U$ date of two perovskite fractions is given (1 and 2). See Fig. 1 and Table 1, and text for further details.

ite/cabonatite and mela-aillikite magmatism occurred over a 20-Myr time span between ca. 600 and 580 Ma. However, the $^{40}Ar/^{39}Ar$ phlogopite age of 550 ± 15 Ma determined for a Torngat aillikite dyke by Digonnet et al. (2000) suggests that deep volatile-rich magmatism continued for an even longer time period.

On the Saglek block, the Hebron mela-aillikite dyke ST263 yielded the oldest $^{206}Pb/^{238}U$ perovskite age (606.0 ± 3.6 Ma) of the UML dykes investigated from the northern Labrador coast, which is similar to the emplacement age of Torngat aillikite Q24. The Eclipse Harbour ST267 (578.2 ± 2.4 Ma) and Killinek Island ST266 (576.4 ± 6.4 Ma) mela-aillikite dykes have identical $^{206}Pb/^{238}U$ emplacement ages similar to Torngat UML Q15 and Q39. The Saglek mela-aillikite ST264 (568.1 ± 3.4 Ma) is the youngest UML dyke known from the northern Labrador coast with an emplacement age that straddles the uncertainty limit of the 'young' $^{40}Ar/^{39}Ar$ age for the Torngat aillikite reported by Digonnet et al. (2000).

Taken together, the new $^{206}Pb/^{238}U$ perovskite ages obtained for aillikite and mela-aillikite dykes from the Torngat Mountains and Saglek block indicate that the entire area was subjected to carbonate-potassic silicate magma production during the Late Neoproterozoic between ca. 610 and 565 Ma. These currently available age data, however, do not allow better resolution of the timing of UML/carbonatite magmatism within this area. Considering the region covered in Fig. 1, time equivalents occur in the Aillik Bay area, central Labrador coast (ca. 590 to 555 Ma; Tappe et al., 2006) and in the Sisimiut–Sarfartoq–Maniitsoq areas of West Greenland (ca. 610 to 550 Ma; Larsen and Rex, 1992; Heaman, 2005) at the southern and northern NAC margins, respectively. In the greater North Atlantic region, Late Neoproterozoic UML/carbonatite occurrences are known from the St. Lawrence Valley Rift system (e.g., Doig and Barton, 1968; Gittins et al., 1975) and the Scandinavian Peninsula (e.g., Doig, 1970; Brueckner and Rex, 1980; Dahlgren, 1994).

5. MAGMA COMPOSITIONS

Major and compatible trace element compositions of the Torngat UML are summarized in Section 2.2 and Fig. 3; more detailed descriptions can be found in Tappe et al. (2004). The new mela-aillikite samples from the Saglek block compositionally resemble their Torngat analogues and mineralogical descriptions are provided as Electronic annex B. All bulk-rock chemical analyses for the Torngat and Saglek block UML are given in Table 2. The bulk-rock Sr–Nd–Hf–Pb as well as carbon and oxygen isotope compositions are listed in Table 3. The complete dataset is available online as Electronic annex A.

5.1. Incompatible elements

Torngat aillikites/carbonatites and mela-aillikites, as well as Saglek block mela-aillikites have high incompatible element abundances with similar primitive upper mantle (PUM; Palme and O'Neill, 2003) normalized element distributions (Fig. 5). They resemble the carbonate-rich type aillikites from Aillik Bay, central Labrador (Tappe et al., 2006, 2007). However, a few subtle but petrogenetically important differences in the incompatible element distribution exist between Torngat aillikites and mela-aillikites on the one hand, and between the Torngat UML and the type rocks from Aillik Bay on the other hand (Fig. 5).

In general, the LFSE, HFSE, and LREE show high concentration levels of up to 700 × PUM, whereas the HREE content is low (below 5 × PUM for Yb and Lu). The LREE/HREE fractionation is extreme in both Torngat aillikites and mela-aillikites with chondrite normalized La/Yb_{CN} ranging between 70 and 180. Pronounced relative depletions occur at K, Pb, Sr–P, and Zr–Hf in a PUM-normalized multi-element diagram, mainly due to the extreme enrichment of similarly incompatible Nb–Ta and the LREE (Fig. 5). A minor trough exists at U, which is in contrast to the U spike in the Aillik Bay pattern.

Torngat aillikites have slightly higher Cs but lower Rb concentrations (lower Rb/Cs; Figs. 6 and 7) at a given K content compared to the majority of mela-aillikites. The characteristic Zr–Hf trough in the aillikite/carbonatite incompatible element pattern ($ZrHf^* = 0.1–0.6$; $ZrHf^*$ defined as PUM-normalized (Zr + Hf)/(Nd + Sm)) is absent from some of the most Ti-rich Torngat and Saglek block mela-aillikites, which have $ZrHf^*$ greater than 0.7 (Figs. 5 and 6). This marked Zr–Hf increase at only slightly increasing Nb–Ta and constant LREE content from aillikites/carbonatites towards carbonate-poor mela-aillikites is furthermore evident from elevated Zr/Nb, Zr/Nd, and Zr/Sm ratios of the mela-aillikites (Fig. 7). The highest $ZrHf^*$ samples have also elevated Rb/Cs (Fig. 6). The Zr/Hf (31–47) and Nb/Ta (8–18) ratios are highly variable; however, no difference is apparent between aillikites and mela-aillikites (Fig. 8). These ratios overlap the range reported for oceanic basalts (cf. Pfänder et al., 2007). Mela-aillikites tend to have slightly higher Nb/U than the majority of aillikites (35–55 vs. 23–43; Fig. 7). Importantly, all Nb/U values are significantly higher than for average continental crust (ca. 8–12; Rudnick and Fountain, 1995) and fall within, or close to, the range of oceanic basalts (47 ± 10; Hofmann et al., 1986).

5.2. Sr–Nd–Hf–Pb isotope composition

The Torngat aillikites/carbonatites and mela-aillikites define an array in Sr–Nd–Hf isotope space between isotopically depleted and enriched end-members (Figs. 9 and 10). Aillikites/carbonatites show a wide range of initial $^{87}Sr/^{86}Sr$ (0.70323–0.70545; Q35 = 0.70713), ε_{Nd} (−3.1 to +1.8; Q35 = −4.9), and ε_{Hf} (−4.8 to +3.5; Q35 = −5.7) values. Although overlapping to a large extent, mela-aillikites have a more restricted, long-term enriched radiogenic isotope composition characterized by negative $\varepsilon_{Nd(i)}$ (−3.9 to −0.5) and $\varepsilon_{Hf(i)}$ (−6.0 to −0.6) at moderately radiogenic $^{87}Sr/^{86}Sr_{(i)}$ (0.70388–0.70523). Aillikite samples with positive ε_{Nd} and ε_{Hf} have higher Fe_2O_3/FeO ratios (>1.7) than the remainder of the Torngat UML suite with negative ε_{Nd} and ε_{Hf} (Fig. 7e). The Saglek block mela-aillikites fall along the Torngat Sr–Nd–Hf isotope array. Mela-aillikites

Table 2
Major (wt%) and trace element (ppm) concentrations of Neoproterozoic carbonatite, aillikite, and mela-aillikite dykes from the Torngat Mountains and the Saglek block, North Atlantic craton, Labrador

Rock type:	Aillikite and carbonatite*															Mela-aillikite																			
Area:	Torngat Mountains															Torngat Mountains																		Saglek block			
Sample No.:	Q9	Q10	Q13*	Q17	Q21	Q24	Q26	Q27	Q29	Q34	Q35	Q37	Q39	Q41	Q42	Q11	Q12	Q14	Q15	Q16	Q18	Q19	Q20	Q22	Q23	Q28	Q30	Q36	Q38	Q40	Q43	ST263	ST264	ST266	ST267
Northing[a]	6585281	6580950	6585198	6565938	6575570	6579365	6543972	6556532	6569574	6590280	6562759	6573475	6545149	6544205	6564722	6582383	6582547	6583052	6574088	6571918	6568781	6585030	6573238	6575551	6575551	6565604	6571253	6573475	6573475	6544143	6557496	6449904	6488375	6698085	6629244
Easting[a]	388941	388336	389251	390704	389970	387839	391523	388392	369952	389828	401981	402227	387348	382650	393850	387109	387018	396748	386034	383866	390228	401156	392341	386053	386053	389184	370604	402227	402227	382774	396993	521840	519589	414773	431424
SiO_2	26.5	29.8	22.0	27.7	28.7	27.4	29.1	26.9	29.2	26.4	23.4	29.3	29.1	27.2	27.5	32.5	34.3	32.3	36.3	35.9	34.1	36.5	37.4	29.9	36.7	33.0	31.9	35.4	35.7	34.1	36.2	35.1	35.5	32.0	32.1
TiO_2	5.82	4.96	4.87	2.45	3.83	5.91	4.39	6.33	7.02	6.28	9.26	5.94	4.79	4.49	3.49	8.23	6.46	4.96	5.21	6.00	7.83	6.33	4.09	9.40	4.60	7.68	7.57	9.42	9.16	5.30	3.85	4.00	3.03	5.15	6.07
Al_2O_3	3.13	4.41	2.94	2.31	2.25	3.49	3.14	3.72	3.64	2.94	4.03	3.63	3.49	2.70	2.26	4.10	4.41	4.36	4.02	5.29	4.33	5.29	5.99	2.94	3.94	4.75	4.66	4.24	4.46	5.05	3.36	2.95	3.18	2.39	4.01
$Fe_2O_3{}^T$	19.0	13.4	15.9	12.1	15.9	18.9	18.6	10.9	15.4	19.4	13.3	18.9	16.5	16.7	14.4	15.8	15.4	15.4	14.6	15.7	18.6	16.9	13.4	17.0	14.2	18.0	15.5	16.6	16.5	14.7	14.5	15.3	14.2	15.0	15.9
MnO	0.26	0.20	0.24	0.23	0.29	0.25	0.27	0.25	0.29	0.29	0.53	0.24	0.28	0.24	0.28	0.22	0.19	0.20	0.19	0.36	0.30	0.24	0.15	0.22	0.26	0.31	0.21	0.30	0.28	0.19	0.20	0.20	0.17	0.20	0.20
MgO	20.0	16.0	16.9	23.9	26.3	20.2	23.1	12.3	16.0	21.3	8.0	18.3	15.4	23.8	20.4	16.6	17.4	19.1	21.8	16.5	16.0	14.9	19.0	23.5	22.1	15.2	14.8	17.9	18.8	14.2	23.2	26.7	28.7	26.1	15.2
CaO	9.68	10.8	9.73	11.3	6.37	10.8	6.15	17.1	11.7	8.95	20.0	12.0	16.1	8.95	12.0	9.09	10.1	11.2	6.73	10.3	8.93	10.9	9.39	6.70	6.33	11.5	12.6	6.71	5.94	12.8	7.61	7.14	5.82	8.52	13.9
Na_2O	0.15	1.12	0.29	0.12	0.18	0.26	0.22	0.28	0.74	0.25	0.20	0.15	0.21	0.17	0.24	0.30	0.63	0.44	0.90	0.61	0.31	0.65	0.87	0.36	1.42	0.38	0.45	0.57	0.50	0.39	0.64	0.78	0.86	0.41	0.73
K_2O	3.14	2.88	2.42	1.40	1.72	2.55	1.76	2.79	2.05	2.94	2.14	2.66	1.90	3.00	2.06	2.92	2.43	2.87	2.51	2.80	3.12	2.56	2.63	2.53	2.28	3.09	2.94	3.49	3.54	2.40	1.74	1.92	1.99	1.85	2.57
P_2O_5	0.86	0.55	0.11	0.18	1.38	0.86	0.62	1.85	0.68	0.68	1.10	1.11	2.95	1.17	1.71	1.14	0.85	0.90	0.59	0.84	1.27	0.80	0.74	0.45	0.72	1.36	0.92	0.46	0.35	1.03	0.84	0.64	0.44	0.47	1.17
$H_2O_{(calc)}$	5.85	3.47	2.28	8.60	9.39	5.38	7.87	1.65	4.03	5.95	3.41	4.57	4.16	3.83	7.51	5.07	4.90	4.38	5.83	3.85	4.13	3.88	4.86	5.93	6.47	3.79	3.64	4.66	4.57	4.77	6.19	3.99	2.25	5.28	2.16
CO_2	5.30	11.80	21.70	8.90	3.50	4.45	4.30	15.00	8.70	4.10	14.10	3.10	3.50	7.10	7.30	3.65	3.00	3.35	0.81	1.76	0.26	0.44	0.66	0.37	1.39	0.48	4.80	0.07	0.00	5.15	1.28	0.48	2.64	2.13	4.70
Total	99.7	99.4	99.4	99.2	99.9	100.3	99.5	99.1	99.4	99.5	99.4	99.9	98.3	99.3	99.1	99.5	100.0	99.5	99.5	99.9	99.2	99.3	99.1	99.3	100.4	99.6	99.9	99.8	99.7	100.0	99.6	99.2	98.8	99.5	98.8
$Fe_2O_3{}^M$	11.9	4.87	11.8	7.84	10.1	11.7	11.4	3.10	8.44	13.0	7.23	11.7	10.3	9.05	8.71	6.73	7.60	8.79	7.70	7.28	10.2	8.97	7.35	13.5	7.90	10.9	6.21	8.23	7.78	6.47	7.01	n.a.	n.a.	n.a.	n.a.
FeO^M	6.32	7.67	2.75	3.84	5.21	6.47	6.48	7.00	6.21	5.74	5.49	6.48	5.58	6.91	5.14	8.13	6.98	5.95	6.23	7.61	7.61	7.09	5.44	3.15	5.68	6.42	8.32	7.48	7.81	7.38	6.74	n.a.	n.a.	n.a.	n.a.
LFSE																																			
Cs	1.53	0.87	0.92	0.69	0.66	1.13	1.03	1.04	0.74	1.12	0.8	1.04	0.72	1.14	0.91	0.98	1.06	1.13	0.68	0.69	1.00	0.55	0.9	0.73	0.64	1.00	0.92	0.86	0.87	0.52	0.41	0.70	0.65	0.91	0.66
Rb	121	131	102	73.2	81.6	114	94.8	130	91.2	103	95.5	105	75.9	128	82.3	138	112	123	101	106	157	96.1	103	115	79.5	162	120	141	141	103	61.5	66.5	79.2	86.4	90.6
Ba	1831	1601	1419	2134	748	1556	1033	1367	1046	1504	1135	1345	1566	1323	911	1297	1033	1646	1046	1362	1487	1420	1517	836	912	1504	1352	1023	1066	1518	689	898	1065	1410	1019
Sr	1451	1127	1460	1570	724	1160	793	1924	762	1157	768	1101	1710	1697	1109	1061	633	814	740	728	1133	1085	1044	748	1223	1090	661	861	614	880	1014	872	799	569	1117
HFSE																																			
Th	25.2	39.3	20.0	57.1	21.9	22.0	19.8	39.9	25.7	18.6	34.5	19.8	43.1*	50.0	19.7	25.9	51.4	38.38	20.3	24.5	33.4	22.2*	21.1	49.8	19.5	29.5	18.8	35.4	31.5	27.4	15.2	12.1	16.2	28.0	14.8
U[b]	5.73*	3.36*	1.59*	7.34	5.24*	4.61*	5.35	4.69*	3.88*	3.45*	4.73*	4.55*	11.7*	8.04	4.98*	5.37*	3.11*	6.66*	2.95*	2.16	6.34*	3.13*	4.49*	8.34*	4.61*	5.83*	3.65	5.3*	4.32	1.97	4.08*	3.1*	2.31*	5.55*	11.6*
Nb	222	247	173	293	184	200	146	345	197	136	117	183	273	311	168	281	166	234	142	112	308	172	188	296	194	273	190	257	206	203	163	100	82.8	199	268
Ta	14.0	18.9	15.1	17.8	15.1	14.2	11.0	20.8	16.8	12.0	12.1	12.8	14.9	22.4	11.9	17.8	19.8	15.7	11.1	14.0	21.5	13.4	11.9	30.5	13.2	20.5	15.6	20.8	17.4	14.2	10.4	9.03	6.19	13.2	17.0
Pb[b]	6.6*	5.8*	7.6*	4.5	7.9*	7.3*	7.8	11.5*	3.1*	11.1*	5.5*	8.2*	24*	9.9	8.3*	4.7*	4.4*	7.4*	7.6*	6.9	21.8*	11.2*	3.9*	6.1*	8*	8.1*	5.9	4*	4.5	9	13.8*	9*	8*	4.8*	7.2*
Zr	616	574	145	144	316	472	263	1134	556	346	513	526	802	610	383	1023	346	671	479	347	1088	774	534	384	702	755	543	1213	895	639	714	410	267	296	747
Hf	15.7	14.7	3.15	4.66	7.64	12.9	6.74	25.7	14.1	9.46	13.8	15.4	25.7	14.3	9.18	24.1	9.61	19.4	12.4	10.5	28.0	19.2	13.0	11.2	16.7	21.7	16.2	31.1	24.9	17.3	15.1	11.6	7.13	11.2	22.8
Y	38.0	30.9	19.3	35.4	26.4	36.2	27.1	50.2	28.7	33.7	47.2	35.9	79.7	48.8	29.2	33.9	26.9	36.5	19.4	22.8	41.1	29.6	30.1	39.7	29.0	41.0	30.4	31.6	26.6	34.9	25.6	17.9	13.9	19.6	30.0
REE																																			
La	232	392	170	405	213	206	127	441	209	171	315	183	494	506	191	248	298	340	161	204	306	195	141	490	188	289	192	282	240	242	145	129	118	227	228
Ce	531	839	421	923	515	475	330	899	516	412	758	378	992	1110	428	558	854	767	348	501	695	468	338	1030	415	643	431	674	577	575	302	239	240	434	411
Pr	51.4	79.3	42.4	92.4	50.1	45.8	39.6	86.8	51.1	43.8	76.2	40.9	96.0	109	47.0	52.2	90.4	72.2	37.3	49.4	67.2	45.4	38.3	100	39.0	61.0	41.6	64.3	55.5	53.6	31.5	25.2	26.5	47.5	43.8
Nd	192	274	159	330	183	171	157	306	189	174	281	152	343	393	175	186	332	249	134	178	239	164	141	360	139	218	151	231	200	191	113	91.8	93.5	176	158
Sm	30.6	37.4	24.1	44.9	27.5	27.8	27.3	43.1	28.6	30.5	42.4	24.6	52.0	56.3	27.0	27.1	43.8	35.5	19.3	25.7	35.3	23.9	21.9	51.9	20.3	33.8	23.7	32.9	28.0	27.3	16.8	14.0	13.9	26.7	23.8
Eu	8.27	9.14	6.06	10.5	7.06	7.56	7.24	10.9	7.39	8.38	10.5	6.76	14.5	13.9	7.11	6.96	9.57	9.23	4.73	6.30	8.33	6.18	5.83	13.2	5.28	9.10	6.43	8.23	6.95	6.94	4.35	3.75	3.38	7.25	6.55
Gd	21.4	24.0	15.3	26.7	18.8	19.3	19.4	29.2	19.0	21.0	28.4	17.6	37.2	33.9	18.0	18.7	26.6	24.2	13.3	16.9	24.3	16.2	15.4	35.6	14.0	23.8	16.9	20.5	17.4	17.3	11.5	9.66	8.16	16.1	16.2
Tb	2.39	2.39	1.59	2.58	2.00	2.23	2.10	3.15	2.08	2.45	3.15	2.06	4.38	3.65	1.93	2.10	2.43	2.58	1.35	1.75	2.68	1.78	1.75	3.62	1.61	2.74	1.91	2.24	1.87	2.05	1.33	1.14	0.89	1.83	2.10
Dy	10.0	9.29	6.08	10.5	7.94	9.40	8.35	13.1	8.62	10.1	13.0	8.99	19.8	15.1	8.28	8.9	9.00	10.61	5.57	7.02	11.5	7.62	7.70	14.3	7.10	11.4	8.01	9.27	7.74	9.09	6.15	4.73	3.71	7.13	8.55
Ho	1.54	1.37	0.88	1.65	1.17	1.48	1.22	2.01	1.32	1.54	2.05	1.43	3.35	2.16	1.27	1.40	1.26	1.62	0.85	1.04	1.80	1.23	1.26	2.01	1.18	1.79	1.29	1.42	1.18	1.45	1.01	0.71	0.51	0.92	1.26
Er	3.26	2.99	1.86	3.79	2.52	3.12	2.38	4.37	2.75	3.06	4.08	2.99	7.41	4.48	2.62	2.96	2.69	3.43	1.89	2.19	3.84	2.78	2.80	4.07	2.60	3.64	2.72	3.07	2.56	3.08	2.27	1.65	1.19	1.88	2.92
Tm	0.34	0.31	0.19	0.45	0.25	0.33	0.24	0.48	0.30	0.33	0.42	0.33	0.87	0.45	0.29	0.32	0.25	0.37	0.21	0.22	0.42	0.32	0.31	0.36	0.31	0.39	0.30	0.36	0.29	0.36	0.27	0.19	0.14	0.18	0.33
Yb	1.79	1.67	0.96	2.47	1.29	1.71	1.20	2.47	1.50	1.69	2.06	1.68	4.64	2.17	1.45	1.72	1.22	1.79	1.14	1.21	2.16	1.79	1.74	1.72	1.63	1.97	1.57	1.95	1.65	1.91	1.46	0.97	0.78	0.91	1.73
Lu	0.19	0.19	0.10	0.29	0.14	0.18	0.12	0.28	0.17	0.20	0.23	0.20	0.56	0.22	0.16	0.19	0.12	0.20	0.14	0.14	0.25	0.23	0.22	0.16	0.19	0.22	0.19	0.25	0.21	0.23	0.18	0.10	0.09	0.10	0.21
TM																																			
Cr	587	999	473	1570	1180	548	1360	484	1110	430	1440	486	463	908	917	826	1460	1320	1330	1250	342	1050	1370	1260	1470	291	834	821	932	845	1150	1240	1520	1630	680
Co	109	83.5	95.9	89.7	112	108	120	58.0	96.0	104	92.5	95	64.3	101	91.8	89.2	100	90	100	96.9	111	99.4	85.5	113	102	95.0	84.2	83.8	83.4	78.7	94.4	101	112	97.7	81.8
Ni	576	586	543	1050	1100	562	904	333	762	453	574	446	230	853	825	651	893	2050	1060	726	570	731	760	1010	1090	462	620	648	672	489	986	984	1150	920	583
Sc	31	26	15	18	18	31	21	31	25	29	30	46	52	19	19	30	29	33	29	30	34	29	26	21	20	37	34	28	30	28	20	19	21	34	28
V	273	285	187	93	175	246	244	302	337	301	376	266	350	149	183	341	265	207	260	328	318	382	266	276	266	308	366	403	369	300	240	264	164	180	335

$Fe_2O_3{}^T$ =total Fe as ferric iron; $Fe_2O_3{}^M$ and FeO^M = ferric and ferrous iron as determined by standard titration techniques and recalculation. $H_2O_{(calc)}$ = calculated difference of 'loss on ignition' and CO_2 content; note that LOI was corrected for oxidation in cases where Fe^{2+} data were available; n.a. = not analyzed. LFSE = Low Field Strength Elements; HFSE = High Field Strength Elements; REE = Rare Earth Elements; TM = Transition Metals.

[a] Coordinates in UTM grid (Zone 20V, NAD83).

[b] U and Pb concentrations with asterisks are ID-TIMS data; remainder are ICP-MS data.

Table 3
Sr–Nd–Hf–Pb and C-O isotope composition of Neoproterozoic carbonatite, aillikite, and mela-aillikite dykes from the Torngat Mountains and the Saglek block, North Atlantic craton, Labrador

	$^{87}Sr/^{86}Sr_m$	$^{a}87Sr/^{86}Sr_i$	$^{143}Nd/^{144}Nd_m$	$^{a}143Nd/^{144}Nd_i$	$^{b}(\varepsilon_{Nd})_i$	$^{c}T^{Nd}_{(DM)}$	$^{176}Hf/^{177}Hf_m$	$^{a}176Hf/^{177}Hf_i$	$^{b}(\varepsilon_{Hf})_i$	$^{c}T^{Hf}_{(DM)}$	$^{206}Pb/^{204}Pb_m$	$^{a}206Pb/^{204}Pb_{(i)}$	$^{207}Pb/^{204}Pb_m$	$^{a}207Pb/^{204}Pb_{(i)}$	$^{208}Pb/^{204}Pb_m$	$^{a}208Pb/^{204}Pb_{(i)}$	$\delta^{13}C_{PDB}$ (‰)	$\delta^{18}O_{SMOW}$(‰)
Torngat carbonatite																		
Q13	0.705230(7)	0.70359	0.512314(7)	0.51196	1.5	1.0	0.282617(40)	0.28257	3.5	1.0	19.73	18.37	15.74	15.65	43.35	37.88	−3.22(2)	12.91(10)
Torngat aillikites																		
Q9	0.705395(7)	0.70344	0.512338(6)	0.51197	1.6	1.0	0.282530(6)	0.28251	1.5	1.0	24.79	18.44	15.99	15.62	47.65	38.74	−5.26(9)	9.49(37)
Q10	0.707266(7)	0.70455	0.512084(6)	0.51177	−2.3	1.2	n.a.	n.a.	n.a.	n.a.	22.39	17.94	15.87	15.60	55.06	38.39	−6.81(1)	13.79(2)
Q17	0.704867(7)	0.70377	0.512276(6)	0.51196	1.4	1.0	0.282602(6)	0.28251	1.4	1.1	n.a.	n.a.	n.a.	n.a.	n.a.	n.a.	−4.29(1)	7.86(2)
Q21	0.706955(7)	0.70431	0.512088(6)	0.51174	−2.9	1.2	0.282379(7)	0.28235	−4.2	1.3	22.45	17.79	15.81	15.54	46.74	40.52	−4.84(1)	11.51(1)
Q24	0.705673(8)	0.70337	0.512336(5)	0.51196	1.4	1.0	0.282540(5)	0.28252	1.8	1.0	22.72	18.33	15.89	15.63	45.33	38.65	−5.23(4)	11.21(17)
Q26	0.706031(8)	0.70323	0.512352(5)	0.51195	1.2	1.0	0.282553(11)	0.28253	2.0	1.0	n.a.	n.a.	n.a.	n.a.	n.a.	n.a.	−4.76(1)	12.18(3)
Q27	0.707032(7)	0.70545	0.512078(5)	0.51175	−2.7	1.2	n.a.	n.a.	n.a.	n.a.	20.70	17.92	15.77	15.60	45.92	38.37	−5.43(1)	13.71(2)
Q29	0.707371(7)	0.70457	0.512160(7)	0.51181	−1.5	1.2	0.282428(8)	0.28241	−2.1	1.2	29.75	18.14	16.23	15.54	64.71	40.16	n.a.	n.a.
Q34	0.705760(7)	0.70366	0.512384(6)	0.51198	1.8	1.0	0.282558(6)	0.28253	2.0	1.0	20.19	18.19	15.72	15.61	41.84	38.39	−5.72(5)	12.80(21)
Q35	0.710044(9)	0.70713	0.511984(6)	0.51164	−4.9	1.4	0.282334(5)	0.28231	−5.7	1.4	24.71	17.81	15.95	15.54	56.53	40.44	−4.94(1)	8.45(1)
Q37	0.705740(7)	0.70349	0.512331(6)	0.51196	1.4	1.0	0.282520(5)	0.28251	1.4	1.0	22.29	18.48	15.86	15.63	44.53	39.22	−5.47(1)	13.78(3)
Q39	0.705323(7)	0.70428	0.512102(4)	0.51175	−2.7	1.2	0.282359(4)	0.28233	−4.8	1.3	21.34	18.10	15.84	15.65	43.37	39.54	−5.15(2)	9.26(2)
Q41	0.706181(7)	0.70441	0.512061(6)	0.51173	−3.1	1.2	0.282360(12)	0.28234	−4.7	1.3	n.a.	n.a.	n.a.	n.a.	n.a.	n.a.	−4.44(1)	11.90(2)
Q42	0.706161(7)	0.70442	0.512101(5)	0.51174	−2.8	1.2	0.282371(5)	0.28234	−4.5	1.3	22.22	17.98	15.83	15.58	47.63	42.26	−4.40(2)	13.10(3)
Torngat mela-aillikites																		
Q11	0.707583(9)	0.70452	0.512068(4)	0.51173	−3.1	1.2	n.a.	n.a.	n.a.	n.a.	26.65	17.76	16.12	15.59	51.44	37.74	−6.88(6)	12.84(12)
Q12	0.708768(7)	0.70463	0.512038(6)	0.51173	−3.0	1.2	0.282335(10)	0.28232	−5.4	1.3	23.51	17.82	15.92	15.58	58.15	28.07	−5.94(3)	14.44(7)
Q14	0.707425(7)	0.70388	0.512160(6)	0.51183	−1.1	1.1	0.282416(9)	0.28240	−2.5	1.2	24.77	17.94	16.01	15.61	50.50	37.92	−5.71(1)	13.35(3)
Q15	0.707588(7)	0.70437	0.512051(8)	0.51172	−3.3	1.2	0.282331(6)	0.28231	−5.5	1.3	20.77	18.12	15.77	15.61	45.98	40.14	−6.56(2)	14.30(4)
Q16	0.707841(7)	0.70443	0.512049(4)	0.51172	−3.4	1.2	0.282320(13)	0.28230	−6.0	1.4	n.a.	n.a.	n.a.	n.a.	n.a.	n.a.	−5.47(4)	12.41(6)
Q18	0.707655(7)	0.70440	0.512126(7)	0.51178	−2.0	1.2	0.282409(5)	0.28240	−2.6	1.2	19.74	17.88	15.69	15.58	41.60	38.48	n.a.	n.a.
Q19	0.706393(7)	0.70432	0.512023(7)	0.51169	−3.9	1.3	n.a.	n.a.	n.a.	n.a.	19.76	17.94	15.73	15.63	42.90	38.79	n.a.	n.a.
Q20	0.706278(7)	0.70397	0.512222(5)	0.51186	−0.5	1.1	0.282477(10)	0.28245	−0.6	1.1	27.13	18.20	16.10	15.57	50.76	37.32	−6.32(1)	14.93(5)
Q22	0.707938(7)	0.70433	0.512063(4)	0.51173	−3.1	1.2	0.282350(6)	0.28233	−5.0	1.3	30.32	17.99	16.33	15.60	62.69	39.16	n.a.	n.a.
Q23	0.706085(7)	0.70453	0.512070(5)	0.51173	−3.2	1.2	0.282341(5)	0.28232	−5.2	1.3	21.96	18.00	15.82	15.59	44.28	38.99	−6.13(6)	14.38(4)
Q28	0.707876(8)	0.70439	0.512121(5)	0.51176	−2.4	1.2	0.282392(4)	0.28238	−3.3	1.2	23.34	18.00	15.85	15.53	50.51	41.90	−5.27(1)	16.11(2)
Q30	0.709492(6)	0.70523	0.512174(6)	0.51181	−1.5	1.2	0.282415(3)	0.28240	−2.6	1.2	n.a.	n.a.	n.a.	n.a.	n.a.	n.a.	−4.92(2)	15.25(3)
Q36	0.708396(7)	0.70456	0.512079(7)	0.51175	−2.7	1.2	0.282346(6)	0.28233	−4.8	1.3	29.84	18.14	16.27	15.58	60.93	35.97	n.a.	n.a.
Q38	0.709780(7)	0.70439	0.512076(4)	0.51175	−2.7	1.2	0.282339(7)	0.28233	−5.1	1.3	n.a.	n.a.	n.a.	n.a.	n.a.	n.a.	n.a.	n.a.
Q43	0.705732(7)	0.70431	0.512076(8)	0.51173	−3.1	1.2	0.282332(8)	0.28233	−4.9	1.3	20.13	18.06	15.66	15.53	48.70	46.25	−4.22(1)	15.59(3)
Saglek block mela-aillikites																		
ST263	0.705687(7)	0.70383	0.512235(5)	0.51187	0.2	1.1	0.282429(10)	0.28241	−1.4	1.2	20.59	18.29	15.57	15.43	41.38	38.51	−5.39(3)	16.04(7)
ST264	0.706639(10)	0.70437	0.512069(5)	0.51173	−3.4	1.2	0.282369(7)	0.28235	−4.5	1.3	19.91	18.08	15.56	15.45	43.13	39.03	−4.82(3)	11.25(3)
ST266	0.707168(7)	0.70365	0.512339(3)	0.51199	1.9	1.0	0.282544(8)	0.28253	2.0	1.0	27.66	18.43	16.06	15.51	54.17	39.28	−5.19(2)	11.94(16)
ST267	0.705753(7)	0.70387	0.512193(4)	0.51185	−0.9	1.1	0.282411(10)	0.28240	−2.7	1.2	30.12	18.20	16.26	15.56	43.06	38.20	−3.22(2)	11.68(3)

Numbers in parentheses are 2σ-of-the-mean errors for individual isotope ratio measurements.

Duplicate Hf isotope data for two samples that had additionally been dissolved in teflon autoclaves are listed in the electronic annex A.

[a] Initial isotope ratios calculated for emplacement ages of 582 Ma (Torngat), 606 Ma (Hebron), 568 Ma (Saglek), 578 Ma (Eclipse Harbour), 576 Ma (Killinek Island).

[b] Initial epsilon Nd values were calculated using ^{147}Sm decay constant of 6.54×10^{-12} year^{-1} (Lugmair and Marti, 1978); $(^{143}Nd/^{144}Nd)_{CHUR} = 0.512638$ (Goldstein et al., 1984); $(^{147}Sm/^{144}Nd)_{CHUR} = 0.1967$ (Peucat et al., 1988). Initial epsilon Hf values were calculated using ^{176}Lu decay constant of 1.865×10^{-11} year^{-1} (Scherer et al., 2001); $(^{176}Hf/^{177}Hf)_{CHUR} = 0.282843$ and $(^{176}Lu/^{177}Hf)_{CHUR} = 0.0342$ (Patchett et al., 2004).

[c] Depleted Mantle model ages $[T^{Nd}_{(DM)}]$ in Ga were calculated using ^{147}Sm decay constant of 6.54×10^{-12} year^{-1}; $(^{143}Nd/^{144}Nd)_{DM} = 0.513150$ (Peucat et al., 1988) and $(^{147}Sm/^{144}Nd)_{DM} = 0.222$ (Michard et al., 1985). Depleted Mantle model ages $T^{Hf}_{(DM)}$ were calculated using ^{176}Lu decay constant of 1.865×10^{-11} year^{-1}; $(^{176}Hf/^{177}Hf)_{DM} = 0.283150$ and $(^{176}Lu/^{177}Hf)_{DM} = 0.034$.

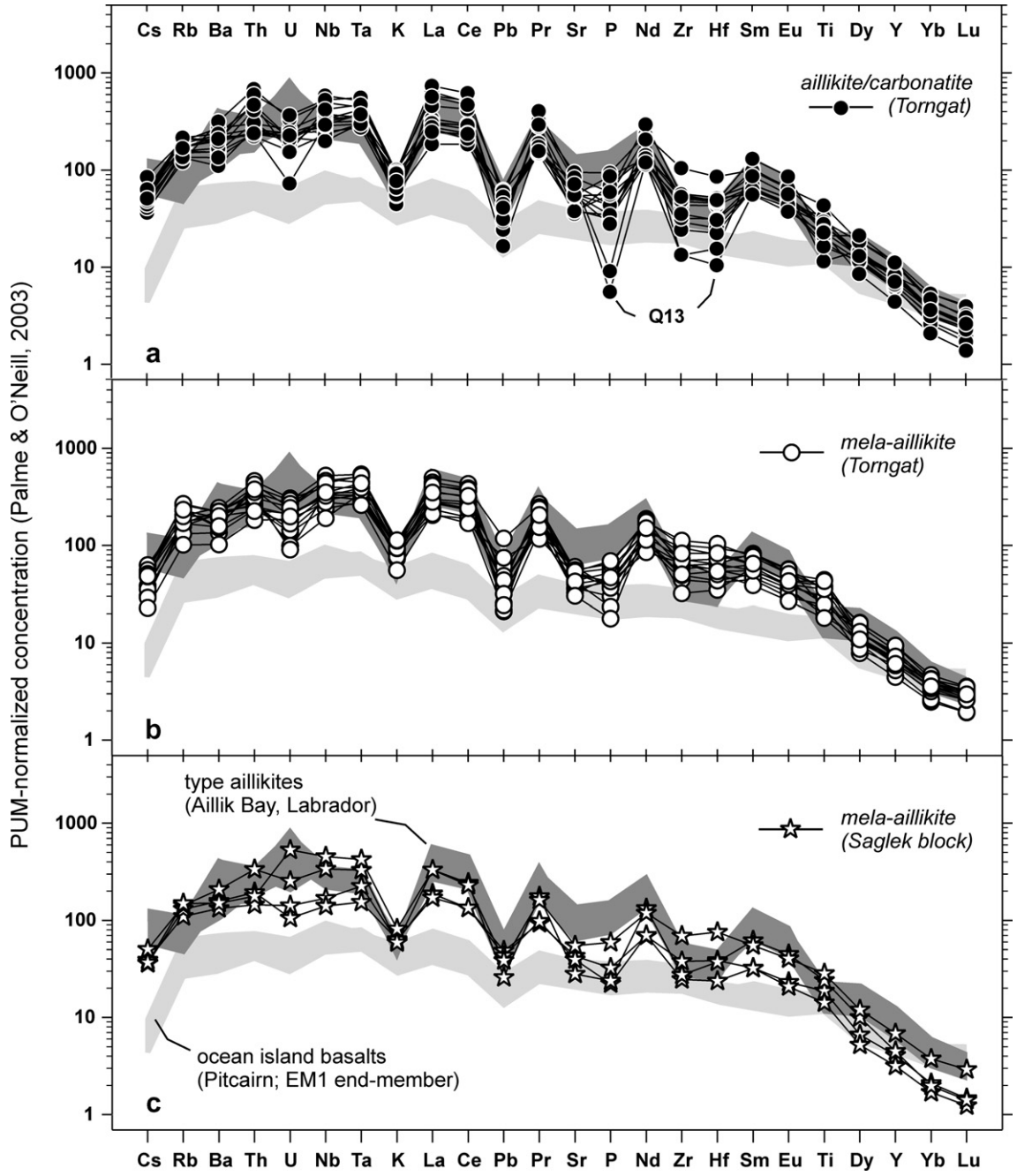

Fig. 5. Primitive upper mantle-normalized (PUM) incompatible element distribution for (a) Torngat aillikites/carbonatites, (b) Torngat mela-aillikites, and (c) Saglek block mela-aillikites. Dark grey field shows the incompatible element pattern of type aillikites from Aillik Bay in central Labrador (Tappe et al., 2006, 2007). Pale grey field displays a typical 'Enriched Mantle' derived ocean island basalt trace element pattern for comparison (Eisele et al., 2002). Note the striking similarity between the various aillikite/mela-aillikite patterns from Labrador with only subtle differences, for example, at Cs–Rb and Zr–Hf. PUM values are from Palme and O'Neill (2003).

ST266 from Killinek Island ($^{87}Sr/^{86}Sr_{(i)} = 0.70361$; $\varepsilon_{Nd(i)} = +2.0$; $\varepsilon_{Hf(i)} = +2.1$) and ST264 from Saglek ($^{87}Sr/^{86}Sr_{(i)} = 0.70437$; $\varepsilon_{Nd(i)} = -3.4$; $\varepsilon_{Hf(i)} = -4.5$) represent the isotopically most depleted and enriched coastal Labrador UML, respectively (Figs. 9 and 10).

The initial Pb isotope compositions of the Torngat aillikites/carbonatites are moderately radiogenic ranging between $^{206}Pb/^{204}Pb_{(i)} = 17.8–18.5$, $^{207}Pb/^{204}Pb_{(i)} = 15.5–15.7$ (Fig. 11), and $^{208}Pb/^{204}Pb_{(i)} = 37.9–40.5$. Torngat mela-aillikite Pb isotope compositions ($^{206}Pb/^{204}Pb_{(i)} = 17.8–18.2$, $^{207}Pb/^{204}Pb_{(i)} = 15.5–15.6$, $^{208}Pb/^{204}Pb_{(i)} = 36.0–41.9$) are less variable and overlap the unradiogenic end of the Torngat aillikite range. The Saglek block mela-aillikites have $^{206}Pb/^{204}Pb_{(i)}$ (18.1–18.3) ratios within the range of the Torngat UML, but importantly they tend to have less radiogenic $^{207}Pb/^{204}Pb_{(i)}$ (15.4–15.6) resembling the urano-

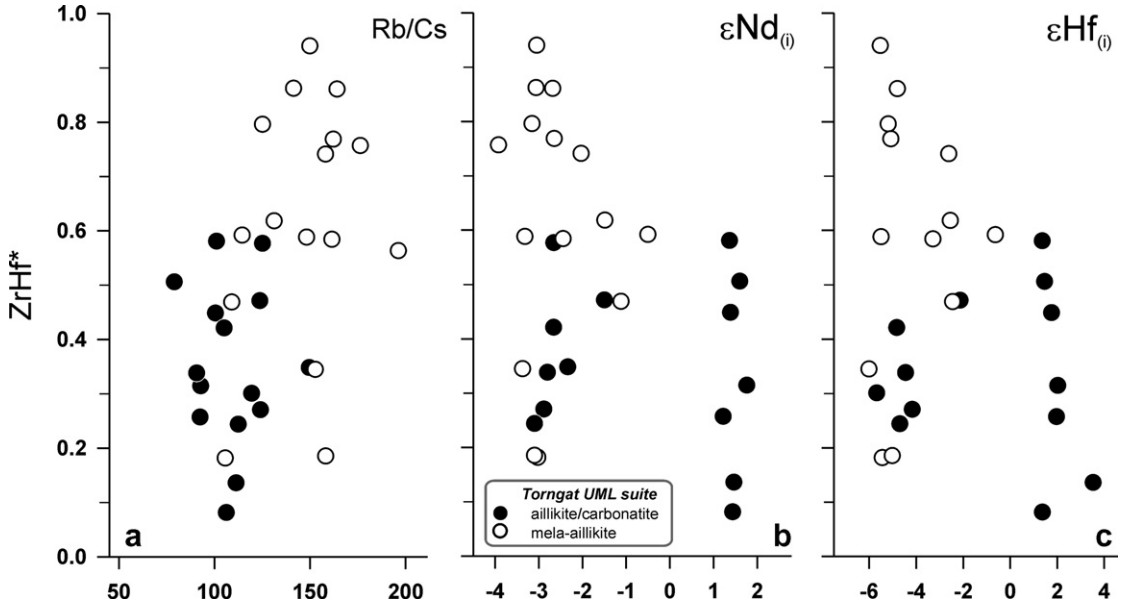

Fig. 6. ZrHf* vs. (a) Rb/Cs, (b) initial εNd, and (c) initial εHf for Torngat aillikite/carbonatite and mela-aillikite dykes from northern Labrador. ZrHf* is an expression of the negative Zr–Hf anomaly in the PUM-normalized incompatible element pattern in Fig. 5 and defined as PUM-normalized (Zr + Hf)/(Nd + Sm). The Saglek block UMLs are not shown for the sake of clarity.

genic Pb isotope composition of aillikites/carbonatites from Aillik Bay on the central Labrador coast (Fig. 11).

5.3. Carbon and oxygen isotope composition

The carbon and oxygen isotope compositions of the Torngat aillikite carbonates range between −6.8 and −4.3‰ $\delta^{13}C_{PDB}$, and +7.9‰ and +13.8‰ $\delta^{18}O_{SMOW}$ (Fig. 12; dolomite carbonatite Q13 = −3.2‰ $\delta^{13}C_{PDB}$). The comparatively small-volume mela-aillikite groundmass carbonates range between −6.9‰ and −4.2‰ $\delta^{13}C_{PDB}$, and +12.4‰ and +16.1‰ $\delta^{18}O_{SMOW}$. Groundmass carbonates of the Saglek (−4.8‰ $\delta^{13}C_{PDB}$; 11.2‰ $\delta^{18}O_{SMOW}$), Killinek Island (−5.2‰ $\delta^{13}C_{PDB}$; 11.9‰ $\delta^{18}O_{SMOW}$), and Hebron (−5.4‰ $\delta^{13}C_{PDB}$; 16.0‰ $\delta^{18}O_{SMOW}$) mela-aillikites fall within the Torngat UML compositional range. Eclipse Harbour mela-aillikite carbonate (−3.2‰ $\delta^{13}C_{PDB}$; 11.7‰ $\delta^{18}O_{SMOW}$) compositionally resembles the Torngat dolomite carbonatite Q13; these carbonates contain isotopically heavier carbon than their Torngat UML analogues (Fig. 12). The isotopically most primary 'mantle-like' Torngat aillikite carbonates overlap the carbon and oxygen isotope composition of carbonates from type aillikites at Aillik Bay in central Labrador (Tappe et al., 2006).

6. DISCUSSION

Aillikite/carbonatite and mela-aillikite magma production occurred beneath the Torngat Mountains and the Saglek block along the western NAC margin between ca. 610 to 565 Ma (Figs. 1, 4). This UML magmatism was contemporaneous with long lasting aillikite and carbonatite igneous activity in the Aillik Bay area, central Labrador (ca. 590 to 555 Ma), and the Sisimiut–Sarfartoq–Maniitsoq areas of western Greenland (ca. 610 to 550 Ma) at the southern and northern NAC margins, respectively. Some of the Torngat and West Greenland UML/carbonatite dykes have been confirmed to contain diamonds (Digonnet et al., 2000; Nielsen and Jensen, 2005; Tappe et al., 2005). Furthermore, Bizzarro and Stevenson (2003) demonstrated that garnet peridotite xenoliths recovered from the West Greenland examples had last equilibrated at pressures of up to 6.3 GPa. Thus, UML and carbonatite magma production beneath the NAC occurred, at least in some areas, at depths greater than 150 km, i.e., well within the diamond stability field.

In the following discussion we place constraints on the heterogeneities within the deep source region of the Torngat UML suite as revealed by their wide range of Sr–Nd–Hf–Pb isotope compositions. An attempt is made to assign the contrasting isotopic components to discernable mineral assemblages and to shed light onto the melting mechanisms by which these components/assemblages were mobilized producing the aillikite/carbonatite and mela-aillikite continuum.

6.1. Source mineralogical control on aillikite/carbonatite and mela-aillikite magma compositions

6.1.1. High Mg and compatible trace elements

Despite the distinctly different carbonate modes and SiO_2, Al_2O_3, Na_2O contents of the Torngat aillikites/carbonatites and mela-aillikites, their high MgO, Ni, and Cr contents overlap and meet the criteria for near-primary peridotitic mantle-derived magmas (e.g., Mg# > 68; Ni > 320 ppm; cf. Frey et al., 1978). Furthermore, the Torngat aillikites, as well as many other carbonate-rich UML from Labrador and West Greenland, broadly resemble near-solidus melt compositions experimentally produced from synthetic carbonate-bearing peridotite in the

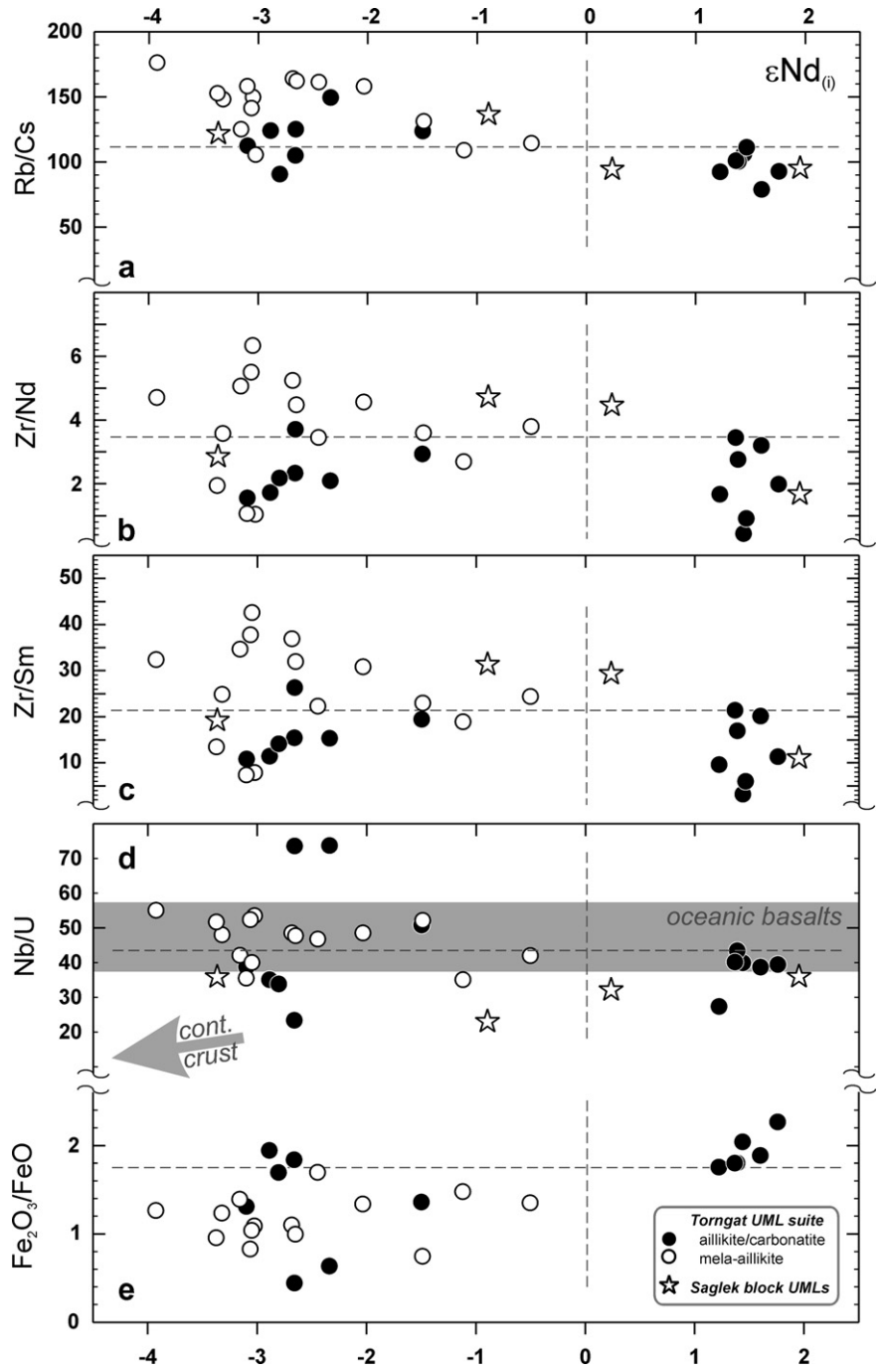

Fig. 7. Incompatible element ratios (a–d) and Fe_2O_3/FeO ratios (e) vs. initial εNd of the Torngat and Saglek block aillikite/carbonatite and mela-aillikite dykes. The grey band shows the range of Nb/U ratios for oceanic basalts (Hofmann et al., 1986). The arrow points towards the compositions of typical continental crust lithologies from cratonic areas. The dashed lines are visual aids enabling a better recognition of the subtle trace element differences between the isotopically depleted (positive εNd) and enriched samples (negative εNd). See text for further explanations.

CMAS–CO_2 system at 6 GPa (Dalton and Presnall, 1998) (Fig. 3). Although these experiments have limitations as to their applicability to natural magmas, because important components such as alkalis, H_2O, FeO, TiO_2, and P_2O_5 are lacking, they demonstrate that partial melts produced from garnet peridotite under CO_2-rich high-pressure conditions can have intermediate compositions between carbonate and ultramafic silicate melts. It is important here to note that the primitive CO_2-poor Torngat mela-aillikites are different in some respects from these CMAS-CO_2 experimental melt compositions; they have higher Al_2O_3 and lower MgO and CaO than the high-pressure run products at a given SiO_2 content (Fig. 3). However, mela-aillikite major element compositions (e.g., SiO_2, TiO_2, Al_2O_3, CaO, and

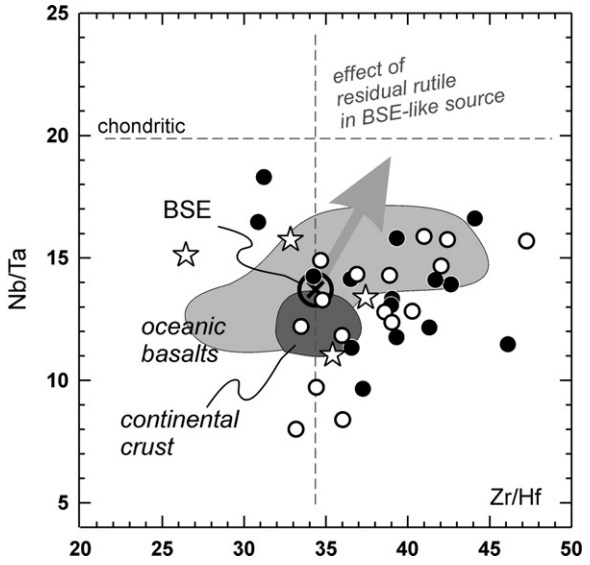

Fig. 8. Nb/Ta vs. Zr/Hf ratios for Torngat and Saglek block aillikite/carbonatite and mela-aillikite dykes from northern Labrador. Despite significant variability in these HFSE ratios, no differences are apparent among the UML types. Fields for oceanic basalts and continental crust materials are shown for comparison (Pfänder et al., 2007). The arrow indicates a presumed trend of a melt formed in the presence of residual rutile with Bulk Silicate Earth-like (BSE) Nb/Ta and Zr/Hf.

alkalis) are similar to melts produced experimentally from a synthetic Ti-rich hydrous ultrabasic glass at 4 and 8 GPa (Konzett, 1997) (Fig. 3). This concordance strongly implies enhanced involvement of trace mineral assemblages ('veins') within peridotite during magma generation, as also suggested by a reconnaissance high-pressure melting experiment on a melilite-bearing UML from Antarctica (Foley and Andronikov, 2003).

The high MgO of the Torngat UMLs is coupled to extremely high incompatible element concentrations (i.e., up to 700 × PUM for the LREE), which are unlikely to be attained by partial melting of peridotite alone, not even at reasonably low degrees of partial melting within an incipient melting regime (Green and Falloon, 1998). This apparent conflict can be readily explained by the presence of mixed source rocks (Irving, 1980; Menzies, 1983; Foley, 1992a,b; Harte et al., 1993), where the vast majority of incompatible elements reside in non-peridotitic trace minerals such as phlogopite, Ti-oxides, and apatite (among others) that have been reported from composite mantle xenoliths. Hence, the Rb–Sr, Sm–Nd, Lu–Hf, and U–Th–Pb radiogenic isotope systems utilized here are unlikely to fingerprint signatures from a pure peridotite substrate, for which Os isotope compositions would be more suitable (Carlson et al., 1996, 2007). Rather, they provide time-integrated information about the metasomatic component(s) in the mantle source region.

The large spread in Torngat aillikite/carbonatite and mela-aillikite Sr–Nd–Hf–Pb isotope ratios (Figs. 9–11), with marked correlations between isotope systems, clearly reflects that more than one mantle source enrichment event had occurred during the protracted geologic history of the NAC. However, the strong similarity of the incompatible element distribution among UML types (Fig. 5) requires that multiple metasomatic overprinting of the peridotite substrate had produced some common trace element-rich minerals, which controlled incompatible element partitioning during both aillikite and mela-aillikite melt production. In order to better understand the metasomatic history of the Torngat UML magma source region, we now explore the nature of potential metasomatic minerals by integration of petrologic, geochemical, and isotopic information retrieved from the observed magma compositions.

6.1.2. High K and LFSE

Aillikite/carbonatite and mela-aillikite magma clearly segregated from a mantle source region that contained an early melting hydrous K-bearing phase. Phlogopite and K-richterite are known from metasomatized mantle assemblages (Dawson and Smith, 1977; Waters, 1987; Ionov and Hofmann, 1995; Grégoire et al., 2002, 2003), both being stable to pressures above 7 GPa (Sudo and Tatsumi, 1990; Foley, 1991; Konzett et al., 1997; Konzett and Ulmer, 1999). Phlogopite is considered the most likely K-bearing phase in the melting assemblage of aillikites because of its potential to produce silica-undersaturated melts with extremely high K_2O/Na_2O ratios (11 ± 5 for Torngat aillikites). In contrast, K-richterite was demonstrated to melt out close to the solidus of ultramafic assemblages, yielding SiO_2-richer melt compositions that are more akin to lamproites (Konzett, 1997; Foley et al., 1999). The Torngat mela-aillikites show exactly this increase in SiO_2 (Fig. 3), as well as lowered K_2O/Na_2O (6 ± 3), that would be expected if K-richterite enters a carbonate-rich melt similar to aillikite. However, K_2O of the mela-aillikites is near-constant (2.7 ± 0.5 wt%) and overlaps the aillikites (2.4 ± 0.5 wt%), which indicates buffering by residual phlogopite during melt segregation. We reach this conclusion because K is a stoichiometric component in phlogopite and the K_2O content in the melt will be near-constant as long as this phase is residual and the melting mode remains constant. Accordingly, K varies mainly as a function of the proportion to which phlogopite enters the melt. The K_2O content of a melt in equilibrium with mantle phlogopite which melts to an extent of ~20-50% (Greenough, 1988) is ~1.6-5 wt%. The average K_2O contents of aillikite and mela-aillikite are at the lower end of this range, which is consistent with lower K-saturation levels in SiO_2-poor melts produced under CO_2-rich conditions (Mengel and Green, 1989; Rogers et al., 1992). Note that phlogopite precipitation from aillikite and mela-aillikite magma en route to the surface can be ruled out as the principle cause for the relatively low K_2O contents, because of their high MgO contents and the presence of mantle-derived materials such as diamond, which is indicative of rapid magma ascent.

The impact of residual phlogopite on the incompatible element patterns of aillikites and mela-aillikites is clearly seen at the relative depletions of Cs and Rb, and the pronounced trough at K and Pb if compared to the highly incompatible HFSE (Th, U, Nb, Ta) and LREE (Fig. 5). The higher Rb/Cs of the majority of mela-aillikites com-

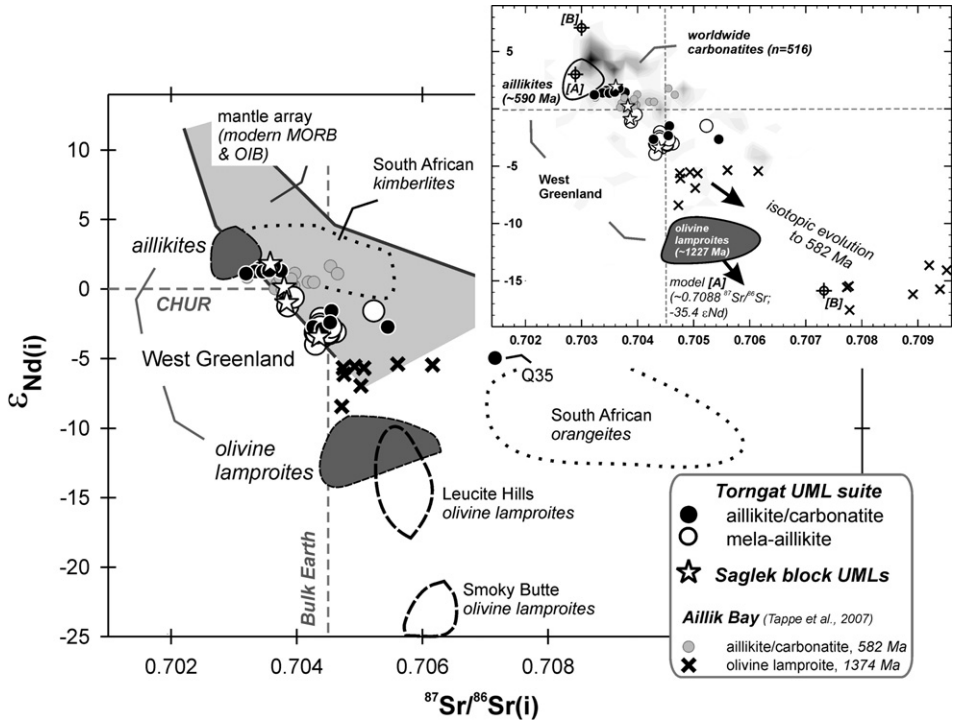

Fig. 9. Initial εNd vs. $^{87}Sr/^{86}Sr$ for Torngat and Saglek block aillikite/carbonatite and mela-aillikite dykes from northern Labrador. The inset shows the new Torngat isotope data in relationship to our choice of end-member compositions utilized for binary mixing calculations as illustrated in greater detail in Fig. 14 and Table 4. ***Model A*** interprets the Torngat aillikite/carbonatite and mela-aillikite compositional continuum as binary mixtures between melts derived from long-term mildly depleted (worldwide carbonatites) and strongly enriched (West Greenland olivine lamproite) isotope end-member components. A similar approach was adopted in ***model B***, where the long-term depleted end-member is represented by the most depleted carbonatite that has yet been reported (Kola Alkaline Province) and the enriched end-member by central Labrador Aillik Bay olivine lamproite derived from ancient hydrous metasomatized SCLM. Fields for West Greenland aillikites and olivine lamproites (Nelson, 1989), Leucite Hills and Smoky Butte olivine lamproites (Fraser et al., 1985), and South African kimberlites and orangeites (Nowell et al., 2004) are shown for comparison. Data for the aillikite/carbonatites and olivine lamproites from Aillik Bay can be found in Tappe et al. (2007).

pared to aillikites at a similar K concentration level (Fig. 6a) could have been produced by the inferred K-richterite fusion, because $^{Krcht/melt}D_{Rb}$ is almost two orders of magnitude lower than $^{phl/melt}D_{Rb}$ (Foley et al., 1996; Tiepolo et al., 2003). However, Cs and Rb concentrations of this phase are an order of magnitude lower than in mantle phlogopite (Grégoire et al., 2002), which is an essential phase during both aillikite and mela-aillikite magma production. Moreover, K-richterite is almost certainly consumed during partial melting (Konzett, 1997; Foley et al., 1999), and so does not buffer the incompatible element distribution. Thus, the difference in Rb/Cs may indicate the presence of distinct phlogopite populations with variable Rb and Cs concentrations. Such differences in the trace element content among distinct phlogopite populations may be the result of growth from contrasting metasomatic agents (i.e., hydrous- vs. carbonate-dominated) during multiple metasomatic events, which are known to have overprinted the cratonic mantle in the region (Griffin et al., 2004; Tappe et al., 2007). This interpretation is consistent with a slightly negative correlation between Rb/Cs and εNd (Fig. 7a) implying the high Rb/Cs signature of mela-aillikites, and some aillikites, fingerprints an old hydrous metasomatized mantle lithology (phlogopite- and K-richterite-bearing) as opposed to a younger phlogopite-bearing metasomatic assemblage that largely contributed to the aillikite/carbonatite magma.

6.1.3. High Ti and HFSE

The extremely high TiO_2 concentrations of aillikites (5.3 ± 1.6 wt%) and mela-aillikites (6.6 ± 1.9 wt%) cannot be explained solely by melting Ti-rich silicates such as phlogopite (cf. Konzett, 1997). As this high TiO_2 is coupled to extremely high Nb–Ta abundances (213 ± 68 and 212 ± 58 ppm Nb, respectively; $>200 \times$ PUM), an early melting Ti-rich oxide phase seems to have largely contributed to the HFSE budget during melt production. Melting experiments on non-peridotitic ultramafic assemblages showed that ilmenite melts out quickly, whereas rutile persists to higher temperatures (Foley et al., 1999). This observation makes ilmenite the more likely Ti-phase that contributed to both aillikite and mela-aillikite magmas accounting for the similar high levels of Ti, Nb–Ta, and Zr–Hf in these rock types (Fig. 5). Furthermore, both the Nb–Ta and the Zr–Hf pair are mildly compatible with ilmenite/melt partition coefficients close to unity (Klemme et al., 2006), which is consistent with the absence of significant Nb/Ta and Zr/Hf fractionation in the aillikite and

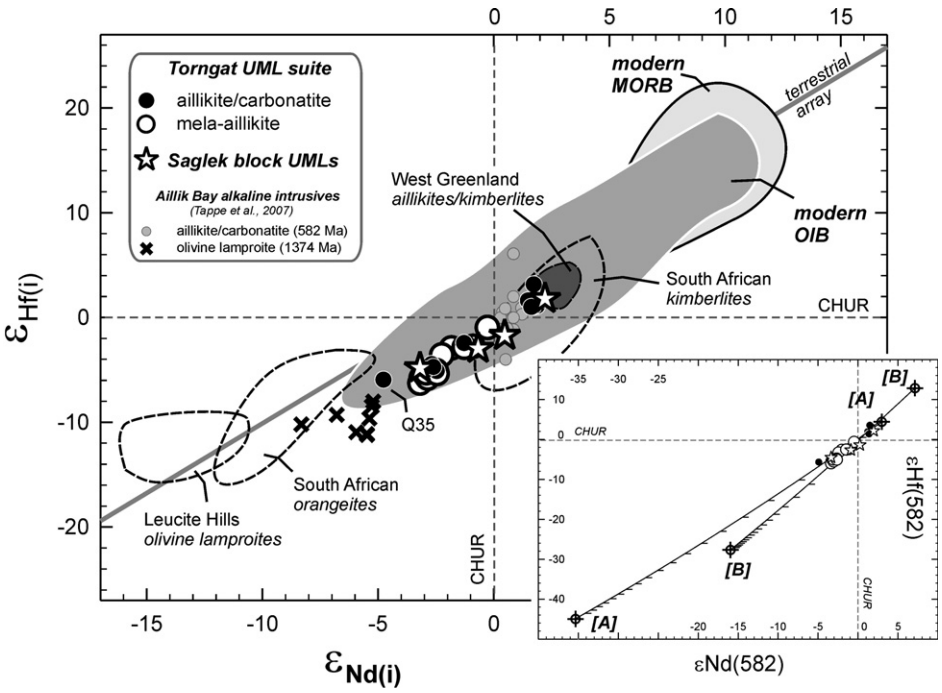

Fig. 10. Initial εHf vs. εNd for Torngat and Saglek block aillikite/carbonatite and mela-aillikite dykes from northern Labrador. The inset shows two mixing hyperbolae (***model A*** and ***B***; see Figs. 9, 14, and Table 4) constructed between isotopically depleted radiogenic components (proxy for convective mantle-derived carbonate melt) and isotopically enriched unradiogenic components (proxy for hydrous metasomatized cratonic mantle-derived potassic melt). The underlying modelling assumptions are described in the main text and in the caption to Fig. 14. Tick marks are at 5% intervals. Fields for West Greenland aillikites/kimberlites (Gaffney et al., 2007), South African kimberlites and orangeites (Nowell et al., 2004), Leucite Hills olivine lamproites (Salters and Hart, 1991), and modern oceanic basalts (compilation retrieved from http://georoc.mpch-mainz.gwdg.de/georoc/) are shown for comparison. Data for the aillikite/carbonatites and olivine lamproites from Aillik Bay can be found in Tappe et al. (2007). Terrestrial array after Vervoort et al. (1999).

mela-aillikite magmas (Fig. 8). Some mela-aillikites show a marked increase in Ti and Zr–Hf (Fig. 5) accompanied by slightly increasing Nb–Ta contents. This appears to indicate that more ilmenite melted locally, presumably reflecting its heterogeneous distribution within the metasomatic source assemblages. Note that rutile is unlikely to be the source of this additional HFSE contribution to some of the mela-aillikites, because it would have significantly increased the Nb–Ta content and Nb/Ta ratio of the melt (Foley et al., 2000; Klemme et al., 2005), which is not observed (Fig. 8). By analogy to the elevated Rb/Cs of mela-aillikites, Zr/Nd and Zr/Sm ratios and thus the $ZrHf^{*}$ value of mela-aillikites (Fig. 6b and c) show a rough negative correlation with εHf and εNd (Fig. 7b and c). This implies that the additionally fused $HFSE^{4+}$ resided in a Ti-oxide phase, most likely ilmenite, which appears to be part of the old hydrous metasomatic assemblage. It furthermore appears that some of the carbonate-rich aillikites with negative εNd and εHf isotope signatures have assimilated some of this long-term enriched material in a rather erratic fashion given their still low Rb/Cs, Zr/Nd, and Zr/Sm ratios (Fig. 7a–c), as well as low SiO_2 contents (Fig. 3).

6.1.4. High P, LREE, and Th/U

Apatite must be an essential constituent of the source region of aillikites and mela-aillikites given their similarly high buffered P_2O_5 concentrations (1.1 ± 0.7 and 0.8 ± 0.3 wt%). It is among the most important phases in controlling the REE and Th–U budgets of alkaline mantle-derived melts (O'Reilly and Griffin, 2000; Klemme and Dalpe, 2003), and the imprint of residual apatite on the incompatible element patterns of the Torngat UMLs may be seen at the Sr–P trough (Fig. 5). Interestingly, this trough also occurs in the type aillikite pattern from Aillik Bay, but less pronounced. The Torngat UMLs have higher Th/U ratios (U trough) than the Aillik Bay type aillikites (U spike), which have higher modal carbonate contents but otherwise share an identical mineral assemblage (Tappe et al., 2006). Given the strong influence of melt composition (i.e., silica activity) on apatite/melt trace element partitioning (Watson and Green, 1981; Klemme and Dalpe, 2003), the observed difference in Th/U between the UML occurrences may reflect the presence of distinctively different apatite within the metasomatic source assemblages, i.e., apatite populations precipitated from silica-rich hydrous and/or carbonate-rich melts/fluids.

6.2. Origin of the carbonate

The $\delta^{13}C$ values of the aillikite and mela-aillikite carbonate fractions overlap (Fig. 12), with values consistent for primary mantle-derived carbon (Deines, 2002). However, only few aillikite carbonates exhibit mantle-like oxygen isotope compositions, i.e. <9‰ $\delta^{18}O_{SMOW}$ (Clarke et al., 1994;

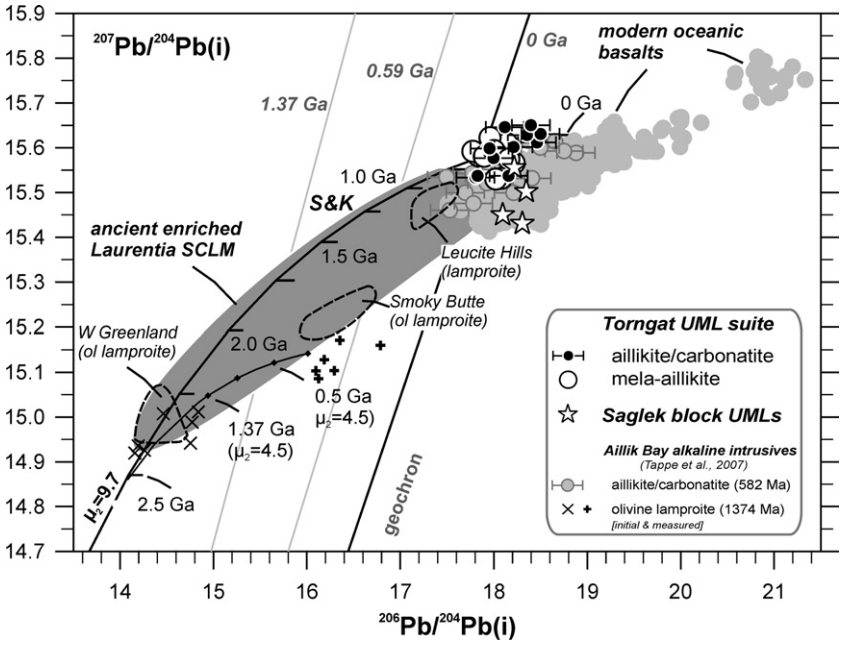

Fig. 11. Initial $^{207}Pb/^{204}Pb$ vs. $^{206}Pb/^{204}Pb$ for Torngat and Saglek block aillikite/carbonatite and mela-aillikite dykes from northern Labrador. The cumulative 2σ uncertainties for the initialized lead isotope ratios are relatively large as indicated by the whiskers for aillikites due to the combined effects of uncertainties from the high measured U/Pb ratios and large age corrections. The Torngat UMLs fall at the end of the Stacey and Kramers (1975) terrestrial Pb evolution curve (tick marks for 250-Myr intervals) close to the present-day geochron. Note the less radiogenic $^{207}Pb/^{204}Pb$ of the Saglek block UMLs compared to their Torngat analogues at similar $^{206}Pb/^{204}Pb$. The Mesoproterozoic olivine lamproites from Aillik Bay in central Labrador and from West Greenland have been interpreted as being derived from a metasomatic SCLM component that was withdrawn from the convective mantle at ca. 2.3 Ga and subsequently evolved with a low second-stage μ_2 (~4.5; Tappe et al., 2007). Such an unradiogenic Pb within ancient metasomatized cratonic SCLM may have imparted low $^{206}Pb/^{204}Pb$ and $^{207}Pb/^{204}Pb$ to the carbonate-rich Torngat aillikites thereby shifting Pb isotope compositions towards mela-aillikites. Ancient enriched Laurentia SCLM as defined by potassic anorogenic magma compositions and micaceous SCLM xenoliths: Fraser et al. (1985), Dudas et al. (1987), Nelson (1989), Carlson and Irving (1994), Peterson et al. (1994), O'Brien et al. (1995), Mirnejad and Bell (2006), and Tappe et al. (2007). Modern oceanic basalt data were compiled from literature and database sources (http://georoc.mpch-mainz.gwdg.de/georoc/). The position of the present-day geochron was calculated for 4.55 Ga and initial Pb isotope composition similar to the Canyon Diablo troilite.

Keller and Hoefs, 1995). The majority of aillikite and all mela-aillikite carbonates have $\delta^{18}O_{SMOW}$ values >9‰, i.e., not in equilibrium with mantle peridotite (5.5 ± 0.5‰; Mattey et al., 1994). Mela-aillikite carbonates tend to be heavier in oxygen, typically >12‰ $\delta^{18}O_{SMOW}$, compared to aillikite carbonates (Fig. 12).

Large variations in $\delta^{18}O$ accompanied by only small variations in $\delta^{13}C$ are known from carbonates in hydrothermally altered systems and volatile-rich ultramafic intrusives such as kimberlites (e.g., Kirkley et al., 1989; Santos and Clayton, 1995; Wilson et al., 2007). The Torngat UML formed rapidly cooled small intrusive dykes that appear pristine down to the microscopic scale with olivine being preserved in most instances (Fig. 2). Furthermore, concentrations of fluid-mobile elements such as Cs and Ba show only a restricted range (Fig. 5) and do not correlate with $\delta^{18}O$. This excludes the possibility of carbonate oxygen isotope overprinting by externally-derived meteoric fluids. Wilson et al. (2007) modelled the closed-system oxygen isotope fractionation between primary kimberlite magmatic carbonates and coexisting magmatic CO_2-H_2O fluids as a function of temperature, fluid CO_2/H_2O ratio, and fluid/solid ratio. They demonstrated the strong influence of the fluid CO_2/H_2O ratio on the magnitude of oxygen isotopic fractionation at temperatures below 750 °C, i.e., along a magmatic cooling path (see temperature scales in Fig. 12). For example, the $\delta^{18}O$ value of primary magmatic carbonate increases from approximately 7.5‰ to 17‰ upon cooling (1100 to 100 °C) in the presence of a H_2O-rich equilibrium magmatic fluid (low molar CO_2/H_2O of 0.25; Fig. 12). In the presence of a CO_2-richer magmatic fluid (CO_2/H_2O of 0.5), however, the isotopic shift is lower (7.5–13‰ $\delta^{18}O$) over the same temperature range (Wilson et al., 2007). These modelled values compare quite well with the observed range of $\delta^{18}O$ values for the Torngat UML suite, i.e., the CO_2-rich aillikites (bulk-rock CO_2/H_2O ratios of up to 5) show generally lower $\delta^{18}O$ values than the H_2O-rich mela-aillikites (CO_2/H_2O of 0.4 ± 0.4; Fig. 12).

Hence, it appears that aillikite and mela-aillikite magmas tapped the same carbonated mantle source region given their 'primitive' overlapping carbonate $\delta^{13}C$ values. The observed variation in the carbonate oxygen isotope data is consistent with sub-solidus (low-temperature) isotope fractionation between this mantle-derived carbonate and magmatic fluids with distinctively different CO_2/H_2O. Our earlier proposal that explained the co-occurrence of carbonate-rich and carbonate-poor UML magma types in the Torngat Mountains by near-surface CO_2-degassing

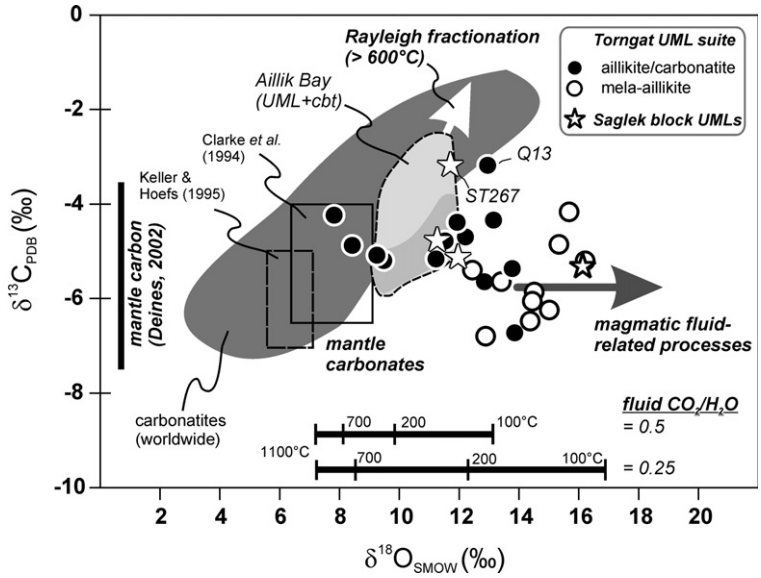

Fig. 12. Carbon and oxygen isotope composition (expressed as ‰ $\delta^{13}C$ and $\delta^{18}O$ relative to PDB and SMOW, respectively) of bulk-rock carbonate fractions from the Torngat and Saglek block aillikite/carbonatite and mela-aillikite dykes from northern Labrador. Open-system CO_2-degassing and concomittant Rayleigh fractionation processes, as well as low-temperature magmatic fluid-related processes have the potential to change primary stable isotope compositions as illustrated by arrows (see Deines, 2002, 2004; Wilson et al., 2007). The temperature scales at the bottom refer to two closed-system isotopic fractionation models between primary magmatic carbonates and magmatic fluids with different CO_2/H_2O. See main text and Wilson et al. (2007) for more details. Dark grey field for worldwide carbonatites was compiled from literature sources and data are available from the first author upon request. An outline for the Aillik Bay aillikite (darker) and carbonatite (paler) bulk-rock carbonates is shown for comparison (Tappe et al., 2006). Symbol size is larger than the 2σ uncertainty.

(Tappe et al., 2004) appears invalid in view of the new isotope data. Such an open-system Rayleigh fractionation process would have produced a significant difference in the carbon isotope composition (Chacko et al., 1991; Ray and Ramesh, 2000; Deines, 2004), which is not observed. Hence this implies that the different bulk-rock CO_2/H_2O ratios and modal carbonate abundances of aillikites and mela-aillikites are inherited from the magma source region. The stable isotope evidence for a primordial origin of the carbon for the CO_2-rich magmatism of the NAC between 610 and 550 Ma (see also Tappe et al., 2006) suggests the recently inferred 'surface' origin of this magmatic carbonate within the 'subducted oceanic crust model' by Gaffney et al. (2007) is incorrect.

6.3. Origins of the depleted and enriched Sr–Nd–Hf isotope components

Torngat aillikites/carbonatites and mela-aillikites form well defined arrays in Sr–Nd–Hf isotope space (Figs. 9 and 10) implying that the peridotite mantle source region contained two isotopically distinct metasomatic assemblages. An isotopically mildly depleted isotope component is identified in some aillikites/carbonatites with initial $^{87}Sr/^{86}Sr \leqslant 0.7038$, $\varepsilon Nd \geqslant +1.2$, $\varepsilon Hf \geqslant +1.4$, and $^{206}Pb/^{204}Pb \geqslant 18.2$ (Figs. 9–11). The extremely high incompatible element concentrations of these primitive carbonate-rich rocks, along with elevated ferric/ferrous ratios, suggest that isotopically depleted oxidized melt was extracted during very low degrees of partial melting of convecting upper mantle material shortly prior to the onset of UML magmatism at ca. 610 Ma. An asthenospheric origin of the carbonate-rich material is in keeping with similar mildly depleted Sr–Nd–Hf isotope compositions of similar old aillikites/carbonatites from central Labrador and West Greenland (Nelson, 1989; Tappe et al., 2006, 2007; Gaffney et al., 2007). This indicates that the extraction of CO_2-rich low-degree melts from the asthenosphere was a widely operating process beneath the NAC lithosphere during the Late Neoproterozoic. However, calculated Nd and Hf depleted mantle model ages for the isotopically depleted aillikites/carbonatites range between 1.0 and 1.1 Ga (Table 3), thus, indicating that an older component is likely to be involved in their genesis.

A long-term enriched isotope component, with initial $^{87}Sr/^{86}Sr > 0.7038$, negative εNd and εHf, and $^{206}Pb/^{204}Pb$ as low as 17.8, is identified in carbonate-poor Torngat mela-aillikites, but importantly, it is also present in some of the aillikites (Figs. 9–11). All of these 'enriched' samples have lower ferric/ferrous ratios than 'depleted' aillikites (Fig. 7e) and their calculated Nd- and Hf-depleted mantle model ages are slightly older (1.1–1.4 Ga). If these model ages represent mixtures of the widely recognized carbonate-rich isotopically depleted component and long-term enriched material, then the enriched 'more reduced' component can be assumed to be significantly older than 1.4 Ga.

Recycled ancient continental crust-derived material can be ruled out as the source of this enriched component given the generally high Ce/Pb and Nb/U of the Torngat UMLs. The Nb/U ratios correlate positively with silica and negatively with εNd (Fig. 7d); an opposite relationship would

be expected if recycled continental crust material represents this isotopically enriched component (Hofmann et al., 1986; Carlson et al., 1996). Furthermore, it should be noted that the initial Sr–Nd–Hf–Pb isotope signatures of mela-aillikites are unlike any of the time-integrated isotope compositions from crustal lithologies in the region (cf. Taylor et al., 1980; Collerson et al., 1989; Blichert-Toft et al., 1999; Vervoort and Blichert-Toft, 1999). This excludes the possibility of a relationship between aillikite and mela-aillikite magmas by assimilation of continental crust en route to the surface.

In Sr–Nd–Hf isotope space, the isotopically most enriched Torngat samples fall near to the Mesoproterozoic Aillik Bay olivine lamproites (Figs. 1, 9, and 10). Moreover, it appears that the enriched mantle component that contributed to the Torngat UML magmas has strong resemblance to the type of isotopically enriched mantle identified in many other North American primitive potassic rock suites such as the West Greenland, Leucite Hills, and Smoky Butte olivine lamproites (Fig. 9). The magma source regions of each of these potassic rock suites must have had a common history of relatively low time-integrated Rb/Sr but extreme LREE and HFSE enrichment (low time-integrated Sm/Nd and Lu/Hf), and it is generally believed that isotopic evolution of certain frozen metasomatic melts/fluids isolated within cratonic mantle lithosphere can develop such peculiar isotope signatures (Fraser et al., 1985; O'Brien et al., 1995; Davies et al., 2006; Mirnejad and Bell, 2006). There is an increasing body of evidence to support the view that minor mantle phases such as metasomatic Ti-oxides and pyroxenitic clinopyroxene are much more likely to be the principal source of negative εHf signatures than peridotitic clinopyroxene and garnet (Pearson and Nowell, 2004; Choukroun et al., 2005), which are the major hosts of Hf in the SCLM (Griffin et al., 2000). A number of studies have demonstrated that peridotitic clinopyroxene and garnet are characterized by extremely radiogenic $^{176}Hf/^{177}Hf$ typically exceeding +10 εHf, even if their Sr and/or Nd isotope compositions indicate long-term enrichment (Schmidberger et al., 2002; Carlson et al., 2004; Ionov et al., 2005; Simon et al., 2007). Note that cratonic eclogites can also be a source of negative εNd and εHf (Jacob et al., 2005), but their trace element budget is too low to cause a significant imprint on the Nd–Hf isotope systematics of highly incompatible element enriched magmas.

Although similar mantle source enrichment patterns with respect to the LFSE (Rb–Sr), LREE (Sm–Nd), and HFSE (Lu–Hf) can be recognized in potassic magmas erupted across Laurentia (Figs. 9 and 10), there are marked differences in terms of the U/Pb evolution, even between neighbouring cratonic segments. This is best illustrated by the less radiogenic $^{207}Pb/^{204}Pb$ of the Saglek block UMLs compared to the Torngat UMLs at similar $^{206}Pb/^{204}Pb$ ratios (Fig. 11), but the origin of this difference is not clear to us at present. Unfortunately, we have no direct age constraints on the timing of the ancient mantle enrichment event that affected the western NAC margin before 1.4 Ga. However, inferences from other regions suggest that there was regionally widespread hydrous metasomatic overprinting of the Laurentian cratonic mantle during the Paleo- and Mesoproterozoic (Dudas et al., 1987; Peterson and LeCheminant, 1993; Morin et al., 2005), e.g. at ca. 1.8 Ga beneath the Wyoming craton (Carlson and Irving, 1994; Rudnick et al., 1999). This period of enhanced mantle overprinting may have been a consequence of failed alkaline magmatism beneath the newly assembled stagnant supercontinent configuration (Hoffman, 1989).

6.4. Petrogenesis of the Torngat ultramafic lamprophyre suite

6.4.1. Physical appearance of deep magma source heterogeneities

An important constraint on the location of the mantle source region comes from the thermal stability of the required source mineralogy. We have pointed out that phlogopite is essential in the melting assemblage of both aillikite and mela-aillikite magmas and this phase, along with many other of the inferred source assemblage minerals, are not stable at convecting upper mantle temperatures (~1480 °C; McKenzie and Bickle, 1988). Phlogopite is stable, however, at P–T conditions of the cooler mantle lithosphere (Mengel and Green, 1989; Sweeney et al., 1993; Konzett, 1997; Ulmer and Sweeney, 2002) and this restricts aillikite and mela-aillikite melt equilibration to cratonic mantle portions (<1400 °C; McKenzie et al., 2005). It does not, however, rule out a contribution from the convecting asthenospheric upper mantle (see previous section), e.g., in the form of metasomatizing melts/fluids.

There exists a general consensus among experimental petrologists that the generation of SiO_2-poor, alkali- and volatile-rich melts cannot be produced by melting of peridotite alone (Arima and Edgar, 1983a,b; Foley, 1992a,b; Konzett, 1997; Ulmer and Sweeney, 2002; Mitchell, 2004). Recently, Foley et al. (2002) and Tappe et al. (2006) have invoked a vein-and-wall rock melting mechanism for the genesis of UML magmas similar to the model developed for the generation of lamproite melts by Foley (1992a). The veins reside in the lower reaches of the peridotite dominated cratonic SCLM and represent frozen convective mantle-derived low-degree melts produced under various oxygen fugacity and volatile conditions (cf. Green et al., 1987), which can lead to a variety of vein compositions (Foley, 1988, 1992b). Whether UML or lamproite magma is produced critically depends on the nature of the vein assemblage, i.e., phlogopite-carbonate dominated veins for aillikites as opposed to phlogopite-richterite-clinopyroxene dominated veins for lamproites. Hence, a plausible scenario for aillikite melt generation could invoke remelting of young phlogopite and carbonate plus minor apatite and Ti-oxide veins in garnet peridotite at the craton base producing potassic, hybrid carbonate—ultramafic silicate magma batches. This mechanism can account for both the thermal stability of the essential hydrous source mineralogy and the juvenile radiogenic isotope signature of aillikites since the veins originate as oxidized low-degree CO_2-rich potassic silicate melts from the convective mantle shortly beforehand and, thus, largely control the incompatible element budget of the magma blend. However, the closely associated mela-aillikites fingerprint more reduced long-term isotopically enriched material within the Torngat

UML magma source region and we have demonstrated that this component most likely resided in an old phlogopite-, K-richterite-, Ti-oxide-, and apatite-bearing assemblage. Such hydrous dominated, Ti-rich metasomatic assemblages are known from many cratons worldwide including the Wyoming and Churchill Provinces of Laurentia (Peterson and LeCheminant, 1993; Carlson and Irving, 1994; Downes et al., 2004). They form part of mantle-derived xenolith suites entrained by volatile-rich mafic/ultramafic magmas and appear to represent reaction products between hydrous alkaline melts of lamproitic composition and cratonic peridotite (Waters, 1987; Sweeney et al., 1993; Konzett et al., 1997; Grégoire et al., 2002; Downes et al., 2004). Rarely observed contact relationships indicate these assemblages form veins and striations within the deeper parts of cratonic lithosphere (Kramers et al., 1983; Waters and Erlank, 1988; Waters et al., 1989; Carlson and Irving, 1994; Rudnick et al., 1999). Among the various hydrous dominated metasomatic assemblages reported, the MARID suite of xenoliths (mica–amphibole–rutile–ilmenite–diopside; Dawson and Smith, 1977) from the Kaapvaal craton is by far the most investigated in terms of geochemistry and phase petrology. MARID nodules are highly enriched in incompatible elements (Kramers et al., 1983; Grégoire et al., 2002) and were shown to have crystallized at pressures higher than 4 GPa (Konzett, 1997; Konzett et al., 1997), i.e., within the diamond stability field. They have extreme isotopic compositions, e.g., rutiles with highly variable εHf ranging between −55 and +110 (Choukroun et al., 2005), testifying to a complex magmatic history.

In short, the above line of reasoning suggests a role for young carbonate-bearing and older hydrous dominated MARID-type vein assemblages in the genesis of the Torngat UML suite. The observed aillikite/carbonatite and mela-aillikite continuum is best explained by the concomitant fusion of these contrasting vein assemblages, which have been introduced into the deep cratonic mantle during previous melting events, but under distinctively different physicochemical conditions due to large-scale structural changes within the NAC lithosphere (Fig. 13).

6.4.2. Course of melting events

As pointed out previously, the isotopically most enriched aillikites and mela-aillikites approach the Sr–Nd–Hf–Pb isotope compositions of olivine lamproites from central Labrador and West Greenland (Figs. 9–11), which were emplaced between 1400 and 1200 Ma. This Mesoproterozoic lamproite magmatism in the NAC region appears to have been confined to the craton margins (Fig. 1). Lead isotopic constraints suggest that melt/fluid-related lithospheric lamproite source enrichment occurred between ca. 2400 and 2100 Ma (Nelson, 1989; Tappe et al., 2007), i.e., during the course of the Paleoproterozoic Laurentia amalgamation. It can be inferred from our isotope data that the MARID-type vein assemblage identified within the Torngat UML magma source region was presumably also produced during this time period (>1400 Ma). This metasome, however, did not produce lamproite magma beneath the Torngat Mountains and the Saglek block during the

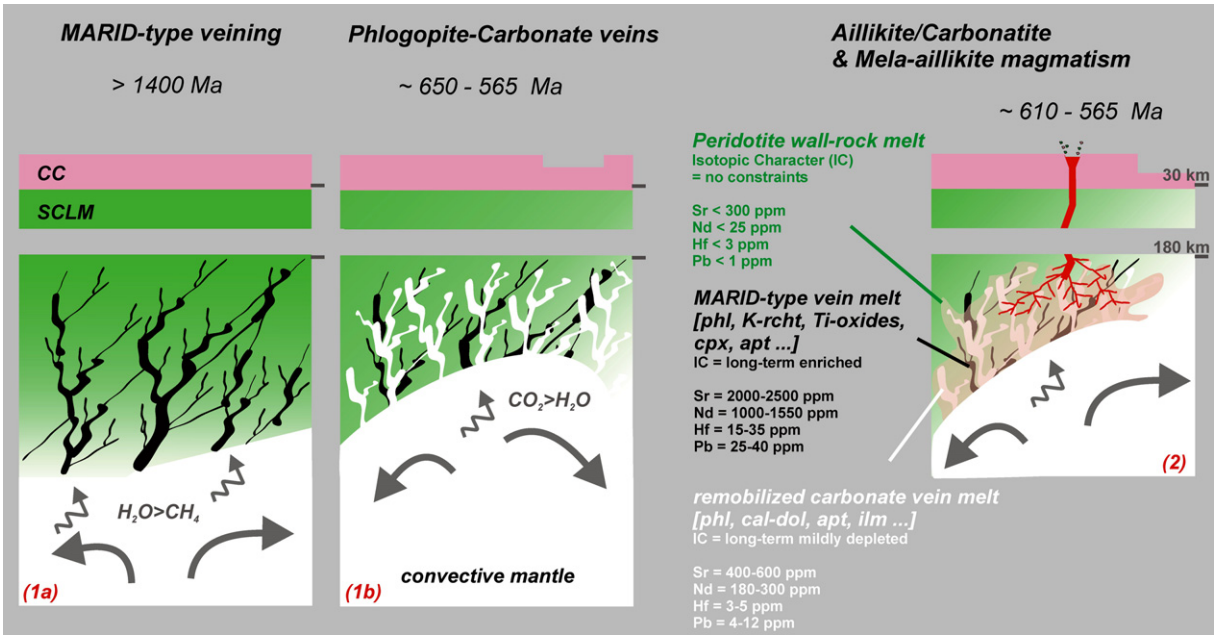

Fig. 13. Cartoon illustrating the petrogenesis of the Torngat aillikite/carbonatite and mela-aillikite compositional continuum. Important steps that may have preconditioned the magma source region and eventually led to the spectrum of hybrid UML magmas encompass: (1a) Formation of MARID-type veins within lower reaches of the NAC lithosphere before ca. 1400 Ma, presumably during the Paleoproterozoic. (1b) Injection of oxidized low-degree CO_2-rich convective mantle-derived melts into this pre-existing more reduced cratonic vein network shortly prior and subsequently to ca. 610 Ma; this produced phlogopite-carbonate dominated veins. (2) Remelting of these carbonate-rich veins, which triggered volatile-fluxed melting of cratonic peridotite and the concomitant fusion of old hydrous MARID-type vein assemblages; this produced the Torngat aillikite/carbonatite and mela-aillikite melt continuum at ca. 610 and 565 Ma.

Mesoproterozoic, presumably owing to a steeper cratonic geotherm in this particular area.

During the Late Neoproterozoic, pronounced stretching and thinning of the North Atlantic cratonic lithosphere occurred throughout contiguous Laurentia and Baltica between ca. 610 and 550 Ma (Doig, 1970; Torsvik et al., 1996). Numerous carbonatite intrusions, many of which are associated with carbonate-rich UML magmas, were emplaced through zones of persistent lithospheric weakness such as the present-day St. Lawrence Valley and Labrador Sea rift systems (Doig and Barton, 1968; Larsen and Rex, 1992; Tappe et al., 2007). The Torngat UML magmatism occurred within this tectonic framework of incipient rifting of thick cratonic lithosphere with low-degree CO_2-rich melt fractions, produced from regionally upwelling convective mantle material, continuously leaking into overlying cratonic mantle peridotite. In addition, these more oxidized CO_2-rich melts may have been preferentially channelled into the pre-existing more reduced MARID-type vein network within the lower reaches of the Torngat cratonic lithosphere, where they solidified as phlogopite-carbonate dominated veins. Continued lithosphere stretching may have caused the quasi-instantaneous remelting of the low-*T* fusible carbonate-rich veins, thereby inducing volatile-fluxed melting of the MARID-type veins and ambient cratonic peridotite, which eventually gave rise to the Torngat aillikite/carbonatite and mela-aillikite melt continuum at 610 to 565 Ma (Fig. 13).

To which side of the compositional continuum a melt batch falls is a function of vein abundances, proportions, and their spatial distribution within the peridotite substrate. We view this rather complex melting scenario as a sequence of incongruent melting reactions affecting a wide range of trace element-rich solid solutions, so that pre-existing differences in the bulk incompatible element distribution between the two metasomatic assemblages will be largely masked (cf. Reiners, 1998). However, the isotopic differences observed within the Torngat UML suite provide compelling evidence for melting of a highly heterogeneous multiply metasomatized mantle source region (Fig. 13). In the following section we will test and quantify this petrogenetic model by means of the available isotope information.

6.5. Quantitative constraints on a possible melting scenario

Important steps that may have preconditioned the Torngat UML magma source region and eventually led to aillikite/carbonatite and mela-aillikite melt production encompass:

(1a) Formation of MARID-type veins within lower reaches of the NAC lithosphere before ca. 1400 Ma, presumably during the Paleoproterozoic; such metasomes have produced lamproite magma elsewhere in the region at ca. 1400 and 1200 Ma.

(1b) Injection of low-degree CO_2-rich convective mantle-derived melts into this pre-existing cratonic vein network shortly prior and subsequently to ca. 610 Ma; this produced phlogopite-carbonate dominated veins.

(2a) Remelting of these carbonate-rich veins, which triggered volatile-fluxed melting of cratonic peridotite at ca. 610 and 565 Ma; this produced 'purest' aillikite melt represented by the isotopically depleted Torngat dykes and phlogopite-poor Sarfartoq dykes, West Greenland.

(2b) Concomitant fusion of the old MARID-type veins into which the CO_2-rich melts were preferentially channelled (see Step 1b); this produced the Torngat aillikite/carbonatite and mela-aillikite melt continuum at ca. 610 and 565 Ma (Fig. 13).

Whereas significant amounts of incompatible elements are pre-concentrated during Steps 1a and 1b, the high-degree partial melt produced from cratonic peridotite during Step 2a seems insignificant in terms of the incompatible element budget of the hybrid UML magmas. Hence, only the isotope compositions of the carbonate-rich and MARID-type veins are considered in a Sr–Nd–Hf–Pb isotope mixing model (Fig. 14). Unfortunately, the curvature of a potential mixing relationship between isotopically depleted and enriched materials, as suggested by the Torngat data, is not sufficient to define the involved end-member compositions by means of the mixing hyperbolae asymptotes (Figs. 9–11). For this reason we have performed isotope mixing calculations between plausible end-member compositions (Fig. 14; Table 4), which will be assessed along with the elemental abundances required below.

It seems reasonable to assign the isotopically depleted carbonate-rich vein component, identified in aillikites/carbonatites, to CO_2-rich convective mantle-derived melts. Our compilation of high-quality Sr–Nd isotope data from more than 500 carbonatites from over 50 worldwide occurrences shows that there is a convergence of the data array towards a cluster between 0.7029 and 0.7037 $^{87}Sr/^{86}Sr$ and from +2.8 to +5.8 εNd (Fig. 9). This indicates that the vast majority of worldwide carbonatites have mildly depleted isotope compositions similar to the Sr–Nd isotope compositions of many ocean island basalts (cf. Nelson et al., 1988). However, one must be cautious when trying to model mixing relationships between melts that formed early in Earth history, i.e., at ca. 610 and 565 Ma, given the isotopic evolution of the crust–mantle system and the fact that the database is dominated by carbonatites younger than 200 Ma. Our 'depleted' end-member choice is therefore twofold: First, we use a 'mildly depleted' Sr–Nd isotope end-member composition that falls at the unradiogenic side of the worldwide carbonatite cluster (model A; $^{87}Sr/^{86}Sr = 0.7029$; $\varepsilon Nd = +3$; Figs. 9, 10, 14). This rather conservative end-member choice is independently supported by similar Sr–Nd isotope compositions of carbonatite and phlogopite-poor aillikite dykes from the Sarfartoq and Maniitsoq areas in West Greenland (Fig. 9; Nelson, 1989), which have ages within the Torngat UML range. Second, we use the most depleted Nd isotope composition of carbonatites yet reported ($\varepsilon Nd = +7.1$; $^{87}Sr/^{86}Sr = 0.7030$), which is viewed as a more extreme scenario (model B; Figs. 9, 10, and 14). These isotopically strongly depleted carbonatites occur in the Sokli and Kovdor complexes (Kramm, 1993; Lee et al., 2006), forming part of the ca. 380-Ma-old Kola Alkaline Province that is known

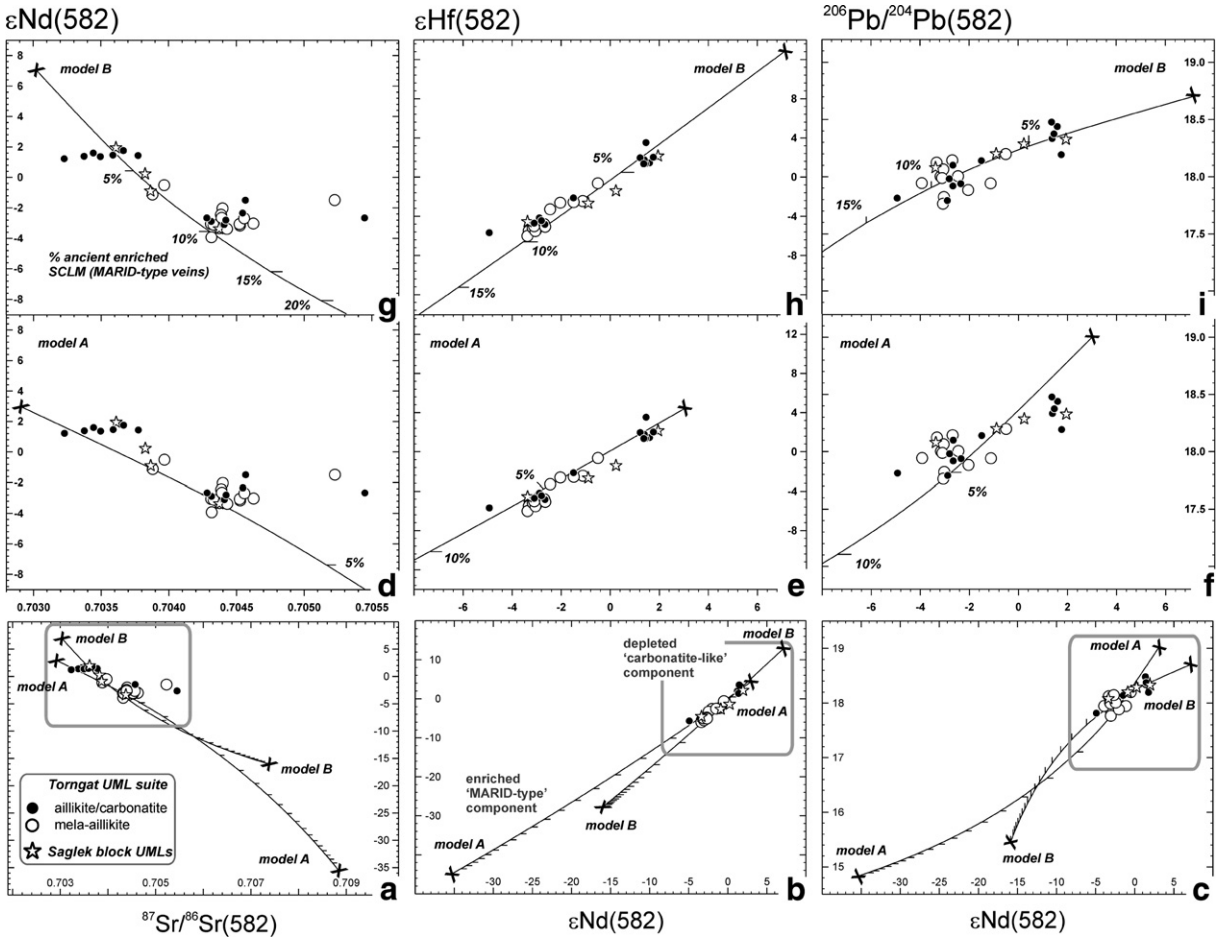

Fig. 14. Combined Sr–Nd–Hf–Pb isotope variation diagrams for Torngat and Saglek block UML dykes from northern Labrador. The bottom panels (a–c) depict our binary mixing ***models A*** and ***B*** in Sr–Nd, Nd–Hf, and Nd–Pb isotope space. Mixing calculations were performed between isotopically depleted 'carbonatite-like' and enriched 'MARID-type' components. Tick marks are for 5% intervals and the chosen end-member parameters are summarized in Table 4. Enlarged portions of the ***model A*** and ***B*** mixing hyperbolae are shown in the middle (d–f) and top (g–i) panels, respectively. This modelling suggests that the incompatible element budget of the majority of aillikite/carbonatite is dominated by a mildly depleted convective mantle-derived component. However, contribution of ca. 5–12% incompatible elements from a long-term enriched isotopically extreme component such as MARID-type veins to the depleted carbonate-rich component can explain the compositional shift from aillikites towards mela-aillikites.

to contain UML intrusives (Beard et al., 1996; Downes et al., 2005).

Mixing hyperbolae can be fit from the two long-term depleted carbonate-rich end-members through the Torngat UML Sr–Nd isotope dataset to 1400- and 1200-Ma-old olivine lamproites from central Labrador ($^{87}Sr/^{86}Sr = 0.7073$; $\varepsilon Nd = -15.9$) and West Greenland ($^{87}Sr/^{86}Sr = 0.7088$; $\varepsilon Nd = -35.4$), which have been time-integrated to 582 Ma (Figs. 9, 14a; the Rb/Sr ratio was corrected for 20% melting-related parent/daughter element fractionation). These lamproite isotope compositions are our best available proxy for the long-term enriched MARID-type component (Nelson, 1989; Tappe et al., 2007), because lamproitic melts were shown experimentally and geochemically to play a crucial role in MARID formation (Waters, 1987; Konzett et al., 1997). Moreover, lamproites represent the only magma type that may exceed the incompatible element concentrations of carbonatite liquids (cf. Foley et al., 1987; Mitchell and Bergman, 1991). This is an essential prerequisite for the melt fraction that carried the isotopically enriched component, because the increase of the Hf concentrations towards some of the most isotopically enriched mela-aillikites (Fig. 6b and c), along with pronounced Sr–Nd-Hf isotope coupling (Fig. 14a and b), requires that the enriched component contributed disproportionately large amounts of these elements to the UML magma blends. Thus, the most extreme lamproite Sr, Nd, Hf, and Pb concentration level was chosen for the long-term isotopically enriched MARID-type component (cf. Mitchell and Bergman, 1991), whereas concentrations from the low end of reported carbonatites were assigned to the long-term depleted component (Table 4).

The Hf isotope composition of our 'mildly depleted' end-member (model A; $\varepsilon Nd = +3$; $\varepsilon Hf = +4.4$) was guided by carbonatite and phlogopite-poor aillikite dyke compositions from Sarfartoq and Maniitsoq, West Greenland (Bizzarro

Table 4
Sr–Nd–Hf–Pb isotope compositions and element concentrations of end-members used in the binary mixing calculations

	Isotopically depleted component				Isotopically enriched component			
	$^{87}Sr/^{86}Sr$	ε_{Nd}	ε_{Hf}	$^{206}Pb/^{204}Pb$	$^{87}Sr/^{86}Sr$	ε_{Nd}	ε_{Hf}	$^{206}Pb/^{204}Pb$
	Proxy for mildly depleted carbonatite (own database)[a]				West Greenland lamproite #5611 (time-integrated to 582 Ma)[c]			
Model A	0.70290 (450)	3.0 (300)	4.4 (4)	19.0 (4)	0.708829 (2500)	−35.4 (1000)	−45 (15)	14.83 (30)
	Most depleted carbonatite (Kola Alkaline Province)[b]				Central Labrador lamproite L68 (time-integrated to 582 Ma)[c]			
Model B	0.703016 (600)	7.1 (200)	12.8 (3)	18.7 (12)	0.707323 (2300)	−15.9 (1550)	−27.6 (35)	15.45 (25)

Numbers in parentheses are elemental concentrations of melts derived from end-member components in ppm. For detailed discussion of the choice of end-member compositions and further explanation see main text.

[a] The mildly depleted carbonatite isotope values are retrieved from our own unpublished carbonatite database (516 analyses from 50 occurrences worldwide ranging in age between Recent and 2000 Ma).

[b] The most depleted Nd isotope compositions of carbonatites are reported from the Kola Alkaline Province (i.e., Sokli and Kovdor carbonatite complexes; Kramm, 1993; Lee et al., 2006).

[c] Isotopic compositions of Aillik Bay (central Labrador; Tappe et al., 2007) and Sisimiut (West Greenland; Nelson, 1989) lamproites are time-integrated to 582 Ma (Rb/Sr was corrected for 20% of parent/daughter element fractionation upon melting).

et al., 2002; Gaffney et al., 2007). The Hf isotope composition of the more depleted end-member (model B; $\varepsilon Nd = +7.1$; $\varepsilon Hf = +12.8$) was chosen by extrapolating εNd to the terrestrial Nd–Hf isotope array of Vervoort et al. (1999) (Figs. 10,14b). This seems reasonable in view of the general paucity of carbonatite Hf isotope data. The West Greenland lamproite εHf values were retrieved in a similar manner ($\varepsilon Nd = -35.4$; $\varepsilon Hf = -45$ at 582 Ma), whereas the Hf isotope composition of the central Labrador olivine lamproites is known ($\varepsilon Nd = -15.9$; $\varepsilon Hf = -27.6$ at 582 Ma; Tappe et al., 2007). The $^{206}Pb/^{204}Pb$ values of the two long-term depleted end-members were assigned as 19.0 for mildly depleted upper mantle (FOZO of Hauri et al., 1994) and 18.7 for the most depleted carbonatites from the Kola Peninsula (Beard et al., 1996; Lee et al., 2006). The $^{206}Pb/^{204}Pb$ ratios of the central Labrador and West Greenland lamproites (15.45 and 14.83 at 582 Ma, respectively) serve as a proxy for the range of Pb isotope compositions of old MARID-type metasomes beneath the NAC margins (Fig. 14c; Nelson, 1989; Tappe et al., 2007).

The following relationship between Torngat aillikites/carbonatites and mela-aillikites is supported by our modelling (Fig. 14d–i; Table 4): Remelting of young phlogopite-carbonate dominated veins triggering volatile-fluxed melting of the surrounding peridotite (Step 2a) can reproduce the isotopic composition of the most depleted aillikites/carbonatites, which appear to have incorporated only very small volumes of the older isotopically enriched MARID-type material ($\leqslant$2–5%). Our data require no more than 5–12% trace element contribution from this MARID-type component to a 'pure' carbonated silicate magma blend (i.e., Sarfartoq aillikites) in order to explain the observed deflection towards more enriched Sr–Nd–Hf–Pb isotope compositions as exemplified by mela-aillikites and some aillikites. This rather restricted MARID contribution to the overall Torngat UML trace element budget is in good agreement with the similar 'carbonatite-like' incompatible element patterns of aillikites/carbonatites and mela-aillikites, with only subtle variations exhibited by the latter (Fig. 5). It furthermore reinforces our suggestion that this MARID-type component is volumetrically small, albeit geochemically and isotopically extreme, and most likely represents an old cratonic vein network (Fig. 13).

7. IMPLICATIONS FOR CRATONIC CARBONATITE AND POTASSIC MAGMATISM

Whereas the majority of carbonate-rich magmas ultimately originate from the convective upper mantle, cratonic potassic magmas are mainly derived from metasomatized lithospheric mantle sources. This relatively straightforward scenario has emerged from experimental and isotopic studies over the past few decades. However, as each craton has a unique metasomatic history, we are left with a proliferation of primitive potassic magma compositions compared to relatively uniform convective mantle-derived magmas such as common basalts and even the less common carbonatites. Further diversification of potassic magma compositions may arise from interactions between cratonic metasomes and convective mantle-derived magmas, which presumably was the impetus for potassic magmatism in a number of alkaline rock provinces.

On the basis of new isotope data for the diamondiferous Torngat ultramafic lamprophyres, we made a case for interaction between ancient MARID-style veined lithospheric mantle, which is a commonly envisaged cratonic lamproite source, and CO_2-rich melts/fluids of carbonatitic affinity invading from the convective asthenospheric mantle. The first conclusion to be drawn from our petrogenetic model is that the carbonate-rich magma production itself appears to be induced by stretching and thinning of the overlying cratonic lithosphere alone. Temperatures at the lithosphere-asthenosphere boundary must have been high enough for carbonate material to melt (>1000 °C), but no higher than 1250 °C (corresponding to a 40 mWm^{-2} cratonic geotherm at ca. 180 km depth) to prevent the MARID-type assemblage from independent 'lamproite' melt generation, which has not occurred beneath the Torngat Mountains. Hence this implies that the ancient MARID-type metasome has been remobilized solely by CO_2-fluxing during the course of regionally widespread extension-related carbonate magmatism between ca. 610 and 550 Ma.

This finding rules out the direct influence of a mantle plume on Late Neoproterozoic UML/carbonatite magma generation within the North Atlantic region as proposed by Tachibana et al. (2006) on noble gas isotopic grounds.

Second, it appears that the low thermal stability of carbonate-bearing assemblages under conditions of the deep cratonic mantle drastically limits the lifetime of carbonate-bearing veins compared to hydrous dominated carbonate-free vein assemblages such as MARID. This difference may help to explain the typically observed contrasting isotope signatures of otherwise similarly strong incompatible element enriched UML/carbonatite and lamproite magmas. Significant long-term radiogenic in-growth is characteristic for the hydrous metasomatic vein assemblages of anorogenic lamproites, whereas it is not facilitated within relatively short-lived carbonate-bearing vein assemblages of cratonic UML/carbonatites.

Third, we concur with Wyllie's (1989) and Eggler's (1989) notion that direct eruption of primary convective mantle-derived carbonatite may be a rare event because our model is consistent with the high potential for CO_2-rich melts to interact with lithospheric mantle. For the North Atlantic craton, we suggest that apart from the initial CO_2 abundances in the source region, the degree of interaction is an important factor in controlling whether CO_2 (i) remains dissolved in carbonated silicate magmas, enabling separation of carbonatite intrusions at crustal levels or (ii) largely reacts out at mantle depths resulting in carbonate-poor, SiO_2-undersaturated UML magmas, as in the Torngat example.

ACKNOWLEDGMENTS

This study was conducted within the DFG project Fo 181/15 (Germany) and manuscript preparation was carried out whilst S.T. was supported by the Humboldt Foundation. Randy Edmunds and Lori Dyson are thanked for logistical support during fieldwork in northern Labrador in 2003. Invitation of S.T. to fieldwork in Greenland by the Geological Survey of Denmark and Greenland in 2006 and 2007 is gratefully acknowledged as it helped to better understand alkaline and carbonatite magmatism across the North Atlantic craton. Karlis Muehlenbachs is thanked for access to his stable isotope facility and Jason Cameron, Gayle Hatchard, and Judy Schultz are thanked for advice during the geochronology work in Edmonton. The manuscript has benefited through the steering efforts of Dejan Prelevic for which we are sincerely grateful. Lotte Larsen, Hugh O'Brien, and Anton le Roex provided detailed and thoughtful reviews that improved the clarity of our argumentation, even if we were not able to address all the questions raised. This is Geological Survey of Canada Contribution 20080897 and Geocycles Publication No. 469.

APPENDIX A. SUPPLEMENTARY DATA

Supplementary data associated with this article can be found, in the online version, at doi:10.1016/j.gca.2008.03.008.

REFERENCES

Arima M. and Edgar A. D. (1983a) High pressure experimental studies on a katungite and their bearing on the genesis of some potassium-rich magmas of the west branch of the African rift. *J. Petrol.* **24**, 166–187.

Arima M. and Edgar A. D. (1983b) A high pressure experimental study on a magnesian-rich leucite-lamproite from the West Kimberley area, Australia: petrogenetic implications. *Contrib. Mineral. Petrol.* **84**, 228–234.

Beard A. D., Downes H., Vetrin V. R., Kempton P. D. and Maluski H. (1996) Petrogenesis of Devonian lamprophyre and carbonatite minor intrusions, Kandalaksha Gulf (Kola Peninsula, Russia). *Lithos* **39**, 93–119.

Bizzarro M. and Stevenson R. (2003) Major element composition of the lithospheric mantle under the North Atlantic craton: evidence from peridotite xenoliths of the Sarfartoq area, southwestern Greenland. *Contrib. Mineral. Petrol.* **146**, 223–240.

Bizzarro M., Simonetti A., Stevenson R. K. and David J. (2002) Hf isotope evidence for a hidden mantle reservoir. *Geology* **30**, 771–774.

Blichert-Toft J., Albarede F., Rosing M. T., Frei R. and Bridgwater D. (1999) The Nd and Hf isotope evolution of the mantle through the Archean: results from the Isua supracrustals, West Greenland, and from the Birimian terranes of West Africa. *Geochim. Cosmochim. Acta* **63**, 3901–3914.

Bridgwater D., Watson J. and Windley B. F. (1973) The Archaean craton of the North Atlantic region. *Philos. Trans. Roy. Soc. Lond.* **273**, 493–512.

Brueckner H. K. and Rex D. C. (1980) K–Ar and Rb–Sr geochronology and Sr isotopic study of the Alnö alkaline complex, northeastern Sweden. *Lithos* **13**, 111–119.

Carlson R. W. and Irving A. J. (1994) Depletion and enrichment history of subcontinental lithospheric mantle: an Os, Sr, Nd and Pb isotopic study of ultramafic xenoliths from the northwestern Wyoming Craton. *Earth Planet. Sci. Lett.* **126**, 457–472.

Carlson R. W., Esperança S. and Svisero D. P. (1996) Chemical and Os isotopic study of Cretaceous potassic rocks from Southern Brazil. *Contrib. Mineral. Petrol.* **125**, 393–405.

Carlson R. W., Irving A. J., Schulze D. J. and Hearn B. C. (2004) Timing of Precambrian melt depletion and Phanerozoic refertilization events in the lithospheric mantle of the Wyoming Craton and adjacent Central Plains Orogen. *Lithos* **77**, 453–472.

Carlson R. W., Araujo A. L. N., Junqueira-Brod T. C., Gaspar J. C., Brod J. A., Petrinovic I. A., Hollanda M. H. B. M., Pimentel M. M. and Sichel S. (2007) Chemical and isotopic relationships between peridotite xenoliths and mafic-ultrapotassic rocks from Southern Brazil. *Chem. Geol.* **242**, 415–434.

Chacko T., Mayeda T. K., Clayton R. N. and Goldsmith J. R. (1991) Oxygen and carbon isotope fractionations between CO_2 and calcite. *Geochim. Cosmochim. Acta* **55**, 2867–2882.

Chakhmouradian A. R. (2006) High-field-strength elements in carbonatitic rocks: geochemistry, crystal chemistry and significance for constraining the sources of carbonatites. *Chem. Geol.* **235**, 138–160.

Choukroun M., O'Reilly S. Y., Griffin W. L., Pearson N. J. and Dawson J. B. (2005) Hf isotopes of MARID (mica-amphibole-rutile-ilmenite-diopside) rutile trace metasomatic processes in the lithospheric mantle. *Geology* **33**, 45–48.

Clarke L. B., Le Bas M. J. and Spiro B. (1994) Rare earth, trace element and stable isotope fractionation of carbonatites at Kruidfontein, Transvaal, South Africa. In *Kimberlites, Related Rocks and Mantle Xenoliths* (eds. H. O. A. Meyer and O. H. Leonardos). Companhia de Pesquisa de Recursos Minerais, Rio de Janeiro, Brazil, pp. 236–251.

Collerson K. D., McCulloch M. T. and Nutman A. P. (1989) Sr and Nd isotope systematics of polymetamorphic Archean

gneisses from southern West Greenland and northern Labrador. *Can. J. Earth Sci.* **26**, 446–466.

Dahlgren S. (1994) Late Proterozoic and Carboniferous ultramafic magmatism of carbonatitic affinity in Southern Norway. *Lithos* **31**, 141–154.

Dalton J. A. and Presnall D. C. (1998) The continuum of primary carbonatitic–kimberlitic melt compositions in equilibrium with lherzolite: data from the system $CaO–MgO–Al_2O_3–SiO_2–CO_2$ at 6 GPa. *J. Petrol.* **39**, 1953–1964.

Davies G. R., Stolz A. J., Mahotkin I. L., Nowell G. M. and Pearson D. G. (2006) Trace element and Sr–Pb–Nd–Hf isotope evidence for ancient, fluid-dominated enrichment of the source of Aldan shield lamproites. *J. Petrol.* **47**, 1119–1146.

Dawson J. B. and Smith J. V. (1977) The MARID (mica–amphibole–rutile–ilmenite–diopside) suite of xenoliths in kimberlite. *Geochim. Cosmochim. Acta* **41**, 309–323.

Deines P. (2002) The carbon isotope geochemistry of mantle xenoliths. *Earth Sci. Rev.* **58**, 247–278.

Deines P. (2004) Carbon isotope effects in carbonate systems. *Geochim. Cosmochim. Acta* **68**, 2659–2679.

Digonnet S., Goulet N., Bourne J., Stevenson R. and Archibald D. (2000) Petrology of the Abloviak aillikite dykes, New Québec: evidence for a Cambrian diamondiferous alkaline province in northeastern North America. *Can. J. Earth Sci.* **37**, 517–533.

Doig R. (1970) An alkaline rock province linking Europe and North America. *Can. J. Earth Sci.* **7**, 22–28.

Doig R. and Barton, Jr., J. M. (1968) Ages of carbonatites and other alkaline rocks in Quebec. *Can. J. Earth Sci.* **5**, 1401–1407.

Downes H., MacDonald R., Upton B. G. J., Cox K. G., Bodinier J. L., Mason P. R. D., James D., Hill P. G. and Hearn, Jr., B. C. (2004) Ultramafic xenoliths from the Bearpaw Mountains, Montana, USA: evidence for multiple metasomatic events in the lithospheric mantle beneath the Wyoming Craton. *J. Petrol.* **45**, 1631–1662.

Downes H., Balaganskaya E., Beard A. D., Liferovich R. and Demaiffe D. (2005) Petrogenetic processes in the ultramafic, alkaline and carbonatitic magmatism in the Kola Alkaline Province: a review. *Lithos* **85**, 48–75.

Dudas F. O., Carlson R. W. and Eggler D. H. (1987) Regional Middle Proterozoic enrichment of the subcontinental mantle source of igneous rocks from central Montana. *Geology* **15**, 22–25.

Edgar A. D. and Vukadinovic D. (1992) Implications of experimental petrology to the evolution of ultrapotassic rocks. *Lithos* **28**, 205–220.

Eggler D. H. (1989) Carbonatites, primary melts, and mantle dynamics. In *Carbonatites: Genesis and Evolution* (ed. K. Bell). Unwin Hyman, London, United Kingdom, pp. 561–579.

Eisele J., Sharma M., Galer S. J. G., Blichert-Toft J., Devey C. W. and Hofmann A. W. (2002) The role of sediment recycling in EM-1 inferred from Os, Pb, Hf, Nd, Sr isotope and trace element systematics of the Pitcairn Hotspot. *Earth Planet. Sci. Lett.* **196**, 197–212.

Foley S. F. (1988) The genesis of continental basic alkaline magmas: an interpretation in terms of redox melting. *J. Petrol.* **Special Lithosphere Issue**, 139–161.

Foley S. F. (1991) High-pressure stability of the fluor- and hydroxy-endmembers of pargasite and K-richterite. *Geochim. Cosmochim. Acta* **55**, 2689–2694.

Foley S. F. (1992a) Vein-plus-wall-rock melting mechanism in the lithosphere and the origin of potassic alkaline magmas. *Lithos* **28**, 435–453.

Foley S. F. (1992b) Petrological characterization of the source components of potassic magmas: geochemical and experimental constraints. *Lithos* **28**, 187–204.

Foley S. F. (1993) An experimental study of olivine lamproite: first results from the diamond stability field. *Geochim. Cosmochim. Acta* **57**, 483–489.

Foley S. F. and Andronikov A. V. (2003) The genesis of ultramafic lamprophyres. Extended Abstracts of the Eighth International Kimberlite Conference, Victoria, Canada, CD-ROM 1–3.

Foley S. F., Taylor W. R. and Green D. H. (1986) The role of fluorine and oxygen fugacity in the genesis of the ultrapotassic rocks. *Contrib. Mineral. Petrol.* **94**, 183–192.

Foley S. F., Venturelli G., Green D. H. and Toscani L. (1987) The ultrapotassic rocks: characteristics, classification, and constraints for petrogenetic models. *Earth Sci. Rev.* **24**, 81–134.

Foley S. F., Jackson S. E., Fryer B. J., Greenough J. D. and Jenner G. A. (1996) Trace element partition coefficients for clinopyroxene and phlogopite in an alkaline lamprophyre from Newfoundland by LAM-ICP-MS. *Geochim. Cosmochim. Acta* **60**, 629–638.

Foley S. F., Musselwhite D. S. and van der Laan S. R. (1999) Melt compositions from ultramafic vein assemblages in the lithospheric mantle: a comparison of cratonic and non-cratonic settings. In *Proceedings of the VIIth International Kimberlite Conference* (eds. J. J. Gurney, J. L. Gurney, M. D. Pascoe and S. H. Richardson). Red Roof Design, Cape Town, pp. 238–246.

Foley S. F., Barth M. G. and Jenner G. A. (2000) Rutile/melt partition coefficients for trace elements and an assessment of the influence of rutile on the trace element characteristics of subduction zone magmas. *Geochim. Cosmochim. Acta* **64**, 933–938.

Foley S. F., Andronikov A. V. and Melzer S. (2002) Petrology of ultramafic lamprophyres from the Beaver Lake area of Eastern Antarctica and their relation to the breakup of Gondwanaland. *Mineral. Petrol.* **74**, 361–384.

Fraser K. J., Hawkesworth C. J., Erlank A. J., Mitchell R. H. and Scott-Smith B. H. (1985) Sr, Nd and Pb isotope and minor element geochemistry of lamproites and kimberlites. *Earth Planet. Sci. Lett.* **76**, 57–70.

Frey F. A., Green D. H. and Roy S. D. (1978) Integrated models of basalt petrogenesis: a study of quartz tholeiites to olivine melilitites from south eastern Australia utilizing geochemical and experimental petrological data. *J. Petrol.* **19**, 463–513.

Gaffney A. M., Blichert-Toft J., Nelson B. K., Bizzarro M., Rosing M. and Albarede F. (2007) Constraints on source-forming processes of West Greenland kimberlites inferred from Hf–Nd isotope systematics. *Geochim. Cosmochim. Acta* **71**, 2820–2836.

Gittins J., Hewins R. H. and Laurin A. F. (1975) Kimberlitic–carbonatitic dikes of the Saguenay River valley, Quebec, Canada. *Phys. Chem. Earth* **9**, 137–148.

Goldstein S. L., O'Nions R. K. and Hamilton P. J. (1984) A Sm–Nd isotopic study of atmospheric dusts and particulates from major river systems. *Earth Planet. Sci. Lett.* **70**, 221–236.

Green D. H. and Falloon T. J. (1998) Pyrolite: a Ringwood concept and its current expression. In *The Earth's Mantle* (ed. I. Jackson). Cambridge University Press, Cambridge, pp. 311–378.

Green D. H. and Wallace M. E. (1988) Mantle metasomatism by ephemeral carbonatite melts. *Nature* **336**, 459–462.

Green D. H., Falloon T. J. and Taylor W. R. (1987) Mantle-derived magmas: roles of variable source peridotite and variable C–H–O fluid compositions. In *Magmatic Processes: Physicochemical Principles* (ed. B. O. Mysen). Geochemical Society, University Park, United States, pp. 139–154.

Greenough J. D. (1988) Minor phases in the Earth's mantle: evidence from trace- and minor-element patterns in primitive alkaline magmas. *Chem. Geol.* **69**, 177–192.

Grégoire M., Bell D. R. and Le Roex A. P. (2002) Trace element geochemistry of phlogopite-rich mafic mantle xenoliths: their

classification and their relationship to phlogopite-bearing peridotites and kimberlites revisited. *Contrib. Mineral. Petrol.* **142**, 603–625.

Grégoire M., Bell D. R. and Le Roex A. P. (2003) Garnet lherzolites from the Kaapvaal Craton (South Africa): trace element evidence for a metasomatic history. *J. Petrol.* **44**, 629–657.

Griffin W. L., Pearson N. J., Belousova E. A., Jackson S. E., van Achterbergh E., O'Reilly S. Y. and Shee S. R. (2000) The Hf isotope composition of cratonic mantle: LAM-MC-ICPMS analysis of zircon megacrysts in kimberlites. *Geochim. Cosmochim. Acta* **64**, 133–147.

Griffin W. L., O'Reilly S. Y., Doyle B. J., Pearson N. J., Coopersmith H., Kivi K., Malkovets V. G. and Pokhilenko N. P. (2004) Lithosphere mapping beneath the North American plate. *Lithos* **77**, 873–922.

Harte B., Hunter R. H. and Kinny P. D. (1993) Melt geometry, movement and crystallization, in relation to mantle dykes, veins and metasomatism. *Philos. Trans. Roy. Soc. Lond.* **342**, 1–21.

Hauri E. H., Whitehead J. A. and Hart S. R. (1994) Fluid dynamic and geochemical aspects of entrainment in mantle plumes. *J. Geophys. Res.* **99**, 24275–24300.

Heaman L. M. (1989) The nature of the subcontinental mantle from Sr–Nd–Pb isotopic studies on kimberlitic perovskite. *Earth Planet. Sci. Lett.* **92**, 323–334.

Heaman L. M. (2005) Patterns of kimberlite emplacement: the importance of robust geochronology. *Report—Geol. Survey Denmark and Greenland* **68**, 25.

Heaman L. M. and Kjarsgaard B. A. (2000) Timing of eastern North American kimberlite magmatism: continental extension of the Great Meteor hotspot track? *Earth Planet. Sci. Lett.* **178**, 253–268.

Hoffman P. F. (1988) United plates of America, the birth of a craton: early Proterozoic assembly and growth of Laurentia. *Annu. Rev. Earth Planet. Sci.* **16**, 543–603.

Hoffman P. F. (1989) Speculations on Laurentia's first gigayear (2.0 to 1.0 Ga). *Geology* **17**, 135–138.

Hoffman P. F. (1990) Dynamics of the tectonic assembly of northeast Laurentia in geon 18 (1.9–1.8 Ga). *Geosci. Can.* **17**, 222–226.

Hofmann A. W., Jochum K. P., Seufert M. and White W. M. (1986) Nb and Pb in oceanic basalts: new constraints on mantle evolution. *Earth Planet. Sci. Lett.* **79**, 33–45.

Ionov D. A. and Hofmann A. W. (1995) Nb–Ta-rich mantle amphiboles and micas: implications for subduction-related metasomatic trace element fractionations. *Earth Planet. Sci. Lett.* **131**, 341–356.

Ionov D. A., Blichert-Toft J. and Weis D. (2005) Hf isotope compositions and HREE variations in off-craton garnet and spinel peridotite xenoliths from central Asia. *Geochim. Cosmochim. Acta* **69**, 2399–2418.

Irving A. J. (1980) Petrology and geochemistry of composite ultramafic xenoliths in alkalic basalts and implications for magmatic processes within the mantle. *Am. J. Sci.* **280**, 389–426.

Jacob D. E., Bizimis M. and Salters V. J. M. (2005) Lu/Hf and geochemical systematics of recycled ancient oceanic crust: evidence from Roberts Victor eclogites. *Contrib. Mineral. Petrol.* **148**, 707–720.

Jaffey A. H., Flynn K. F., Glendenin L. E., Bentley W. C. and Essling A. M. (1971) Precision measurements of half-lives and specific activities of ^{235}U and ^{238}U. *Phys. Rev.* **4**, 1889–1906.

Keller J. and Hoefs J. (1995) Stable isotope characteristics of recent natrocarbonatite from Oldoinyo Lengai. In *Carbonatite Volcanism: Oldoinyo Lengai and the Petrogenesis of Natrocarbonatites* (eds. K. Keller and J. Bell). Springer, Berlin, pp. 113–123.

Kirkley M. B., Smith H. S. and Gurney J. J. (1989) Kimberlite carbonates: a carbon and oxygen stable isotope study. In *Kimberlites and Related Rocks* (ed. J. Ross). Geological Society of Australia, Sydney, NSW, Australia, pp. 264–281.

Klemme S. and Dalpe C. (2003) Trace-element partitioning between apatite and carbonatite melt. *Am. Miner.* **88**, 639–646.

Klemme S., Prowatke S., Hametner K. and Günther D. (2005) Partitioning of trace elements between rutile and silicate melts: implications for subduction zones. *Geochim. Cosmochim. Acta* **69**, 2361–2371.

Klemme S., Günther D., Hametner K., Prowatke S. and Zack T. (2006) The partitioning of trace elements between ilmenite, ulvospinel, annalcolite and silicate melts with implications for the early differentiation of the moon. *Chem. Geol.* **234**, 251–263.

Konzett J. (1997) Phase relations and chemistry of Ti-rich K-richterite-bearing mantle assemblages: an experimental study to 8.0 GPa in a Ti–KNCMASH system. *Contrib. Mineral. Petrol.* **128**, 385–404.

Konzett J. and Ulmer P. (1999) The stability of hydrous potassic phases in lherzolite mantle: an experimental study to 9.5 GPa in simplified and natural bulk compositions. *J. Petrol.* **40**, 629–652.

Konzett J., Sweeney R. J., Thompson A. B. and Ulmer P. (1997) Potassium amphibole stability in the upper mantle: an experimental study in a peralkaline KNCMASH system to 8.5 GPa. *J. Petrol.* **38**, 537–568.

Korstgård J., Ryan B. and Wardle R. J. (1987) The boundary between Proterozoic and Archaean crustal blocks in central West Greenland and northern Labrador. In *Evolution of the Lewisian and Comparable Precambrian High Grade Terrains* (eds. R. G. Park and J. Tarney). Geological Society of London, London, United Kingdom, pp. 247–259.

Kramers J. D., Roddick J. C. M. and Dawson J. B. (1983) Trace element and isotope studies on veined, metasomatic and "MARID" xenoliths from Bultfontein, South Africa. *Earth Planet. Sci. Lett.* **65**, 90–106.

Kramm U. (1993) Mantle components of carbonatites from the Kola alkaline province, Russia and Finland: a Nd–Sr study. *Eur. J. Mineral.* **5**, 985–989.

Larsen L. M. and Rex D. C. (1992) A review of the 2500 Ma span of alkaline-ultramafic, potassic and carbonatitic magmatism in West Greenland. *Lithos* **28**, 367–402.

Lee M. J., Lee J. I., Do Hur S., Kim Y., Moutte J. and Balaganskaya E. (2006) Sr–Nd–Pb isotopic compositions of the Kovdor phoscorite–carbonatite complex, Kola Peninsula, NW Russia. *Lithos* **91**, 250–261.

Lugmair G. W. and Marti K. (1978) Lunar initial ^{143}Nd/^{144}Nd: differential evolution of the lunar crust and mantle. *Earth Planet. Sci. Lett.* **39**, 349–357.

Mattey D. P., Lowry D. and Macpherson C. (1994) Oxygen isotope composition of mantle peridotite. *Earth Planet. Sci. Lett.* **128**, 231–241.

McKenzie D. and Bickle M. J. (1988) The volume and composition of melt generated by extension of the lithosphere. *J. Petrol.* **29**, 625–679.

McKenzie D., Jackson J. and Priestley K. (2005) Thermal structure of oceanic and continental lithosphere. *Earth Planet. Sci. Lett.* **233**, 337–349.

Meen J. K., Ayers J. C. and Fregeau E. J. (1989) A model of mantle metasomatism by carbonated alkaline melts: trace-element and isotopic compositions of mantle source regions of carbonatite and other continental igneous rocks. In *Carbonatites: Genesis and Evolution* (ed. K. Bell). Unwin Hyman, London, United Kingdom, pp. 464–499.

Mengel K. and Green D. H. (1989) Stability of amphibole and phlogopite in metasomatized peridotite under water-saturated

and water-undersaturated conditions. In *Kimberlites and Related Rocks* (ed. J. Ross). Geological Society of Australia, Sydney, NSW, Australia, pp. 571–581.

Menzies M. A. (1983) Mantle ultramafic xenoliths in alkaline magmas: evidence for mantle heterogeneity modified by magmatic activity. In *Continental Basalts and Mantle Xenoliths* (eds. C. J. Hawkesworth and M. J. Norry). Shiva, Nantwich, pp. 92–110.

Michard A., Gurriet P., Soudant M. and Albarede F. (1985) Nd isotopes in French Phanerozoic shales: external versus internal aspects of crustal evolution. *Geochim. Cosmochim. Acta* **49**, 601–610.

Mirnejad H. and Bell K. (2006) Origin and source evolution of the Leucite Hills lamproites: evidence from Sr–Nd–Pb–O isotopic compositions. *J. Petrol.* **47**, 2463–2489.

Mitchell R. H. (1995) Melting experiments on a sanidine phlogopite lamproite at 4–7 GPa and their bearing on the sources of lamproitic magmas. *J. Petrol.* **36**, 1455–1474.

Mitchell R. H. (2004) Experimental studies at 5–12 GPa of the Ondermatjie hypabyssal kimberlite. *Lithos* **76**, 551–564.

Mitchell R. H. (2005) Carbonatites and carbonatites and carbonatites. *Can. Miner.* **43**, 2049–2068.

Mitchell R. H. and Bergman S. C. (1991) *Petrology of Lamproites*. Plenum Press, New York.

Mitchell R. H., Scott-Smith B. H. and Larsen L. M. (1999) Mineralogy of ultramafic dikes from the Sarfartoq, Sisimiut and Maniitsoq areas, West Greenland. In *Proceedings of the VIIth international kimberlite conference* (eds. J. J. Gurney, J. L. Gurney, M. D. Pascoe and S. H. Richardson). Red Roof Design, Cape Town, pp. 574–583.

Morin D., Hébert R. and Corriveau L. (2005) Mesoproterozoic deep K-magmatism recorded in a megacryst- and xenolith-bearing minette dyke, western Grenville Province. *Can. J. Earth Sci.* **42**, 1881–1907.

Münker C., Weyer S., Scherer E. and Mezger K. (2001) Separation of high field strength elements (Nb, Ta, Zr, Hf) and Lu from rock samples for MC-ICPMS measurements. *Geochem. Geophys. Geosyst.* **2**, 2001GC000183.

Nelson D. R. (1989) Isotopic characteristics and petrogenesis of the lamproites and kimberlites of central West Greenland. *Lithos* **22**, 265–274.

Nelson D. R., Chivas A. R., Chappell B. W. and McCulloch M. T. (1988) Geochemical and isotopic systematics in carbonatites and implications for the evolution of ocean-island sources. *Geochim. Cosmochim. Acta* **52**, 1–17.

Nielsen T. F. D. and Jensen S. M. (2005) The Majuagaa calcite–kimberlite dyke, Maniitsoq, southern West Greenland. *Report—Geol. Survey Denmark and Greenland* **43**, 1–59.

Nowell G. M., Pearson D. G., Bell D. R., Carlson R. W., Smith C. B., Kempton P. D. and Noble S. R. (2004) Hf isotope systematics of kimberlites and their megacrysts: new constraints on their source regions. *J. Petrol.* **45**, 1583–1612.

O'Brien H. E., Irving A. J., McCallum I. S. and Thirlwall M. F. (1995) Strontium, neodymium, and lead isotope evidence for the interaction of post-subduction asthenospheric potassic mafic magmas of the Highwood Mountains, Montana, USA, with ancient Wyoming craton lithospheric mantle. *Geochim. Cosmochim. Acta* **59**, 4539–4556.

Olafsson M. and Eggler D. H. (1983) Phase relations of amphibole, amphibole-carbonate, and phlogopite-carbonate peridotite: petrologic constraints on the asthenosphere. *Earth Planet. Sci. Lett.* **64**, 305–315.

O'Reilly S. Y. and Griffin W. L. (2000) Apatite in the mantle: implications for metasomatic processes and high heat production in Phanerozoic mantle. *Lithos* **53**, 217–232.

Palme H. and O'Neill H. S. C. (2003) Cosmochemical estimates of mantle composition. In *Treatise on Geochemistry* (ed. R. W. Carlson). Elsevier, Amsterdam, pp. 1–38.

Patchett P. J., Vervoort J. D., Söderlund U. and Salters V. J. M. (2004) Lu–Hf and Sm–Nd isotopic systematics in chondrites and their constraints on the Lu–Hf properties of the Earth. *Earth Planet. Sci. Lett.* **222**, 29–41.

Pearson D. G. and Nowell G. M. (2004) Re–Os and Lu–Hf isotope constraints on the origin and age of pyroxenites from the Beni Bousera peridotite massif: implications for mixed peridotite–pyroxenite mantle sources. *J. Petrol.* **45**, 439–455.

Peterson T. D. and LeCheminant A. N. (1993) Glimmerite xenoliths in early Proterozoic ultrapotassic rocks from the Churchill Province. *Can. Miner.* **31**, 801–819.

Peterson T. D., Esperanca S. and LeCheminant A. N. (1994) Geochemistry and origin of the Proterozoic ultrapotassic rocks of the Churchill Province, Canada. *Mineral. Petrol.* **51**, 251–276.

Peucat J. J., Vidal P., Bernard-Griffiths J. and Condie K. C. (1988) Sr, Nd, and Pb isotopic systematics in the Archean low- to high-grade transition zone of southern India: syn-accretion versus post-accretion granulites. *J. Geol.* **97**, 537–550.

Pfänder J. A., Münker C., Stracke A. and Mezger K. (2007) Nb/Ta and Zr/Hf in ocean island basalts—implications for crust-mantle differentiation and the fate of Niobium. *Earth Planet. Sci. Lett.* **254**, 158–172.

Ray J. S. and Ramesh R. (2000) Rayleigh fractionation of stable isotopes from a multicomponent source. *Geochim. Cosmochim. Acta* **64**, 299–306.

Reiners P. W. (1998) Reactive melt transport in the mantle and geochemical signatures of mantle-derived magmas. *J. Petrol.* **39**, 1039–1061.

Rivers T., Mengel F., Scott D. J., Campbell L. M. and Goulet N. (1996) Torngat Orogen—a Palaeoproterozoic example of a narrow doubly vergent collisional orogen. In *Precambrian Crustal Evolution in the North Atlantic Region* (ed. T. S. Brewer). Geological Society, London, United Kingdom, pp. 117–136.

Rock N. M. S. (1991) *Lamprophyres*. Blackie & Son, Glasgow.

Rogers N. W., Hawkesworth C. J. and Palacz Z. A. (1992) Phlogopite in the generation of olivine melilitites from Namaqualand, South Africa and implications for element fractionation processes in the upper mantle. *Lithos* **28**, 347–365.

Romer R. L., Heinrich W., Schroder-Smeibidl B., Meixner A., Fischer C. O. and Schulz C. (2005) Elemental dispersion and stable isotope fractionation during reactive fluid-flow and fluid immiscibility in the Bufa del Diente aureole, NE-Mexico: evidence from radiographies and Li, B, Sr, Nd, and Pb isotope systematics. *Contrib. Mineral. Petrol.* **149**, 400–429.

Rudnick R. L. and Fountain D. M. (1995) Nature and composition of the continental crust: a lower crustal perspective. *Rev. Geophys.* **33**, 267–309.

Rudnick R. L., Ireland T. R., Gehrels G., Irving A. J., Chesley J. T. and Hanchar J. M. (1999) Dating mantle metasomatism: U–Pb geochronology of zircons in cratonic mantle xenoliths from Montana and Tanzania. In *Proceedings of the VIIth International Kimberlite Conference* (eds. J. J. Gurney, J. L. Gurney, M. D. Pascoe and S. H. Richardson). Red Roof Design, Cape Town, pp. 728–735.

Salters V. J. M. and Hart S. R. (1991) The mantle sources of ocean ridges, islands and arcs: the Hf-isotope connection. *Earth Planet. Sci. Lett.* **104**, 364–380.

Santos R. V. and Clayton R. N. (1995) Variations of oxygen and carbon isotopes in carbonatites: a study of Brazilian alkaline complexes. *Geochim. Cosmochim. Acta* **59**, 1339–1352.

Scherer E., Münker C. and Mezger K. (2001) Calibration of the Lutetium–Hafnium clock. *Science* **293**, 683–687.

Schmidberger S. S., Simonetti A., Francis D. and Gariépy C. (2002) Probing Archean lithosphere using the Lu–Hf isotope systematics of peridotite xenoliths from Somerset Island kimberlites, Canada. *Earth Planet. Sci. Lett.* **197**, 245–259.

Simon N. S. C., Carlson R. W., Pearson D. G. and Davies G. R. (2007) The origin and evolution of the Kaapvaal cratonic lithospheric mantle. *J. Petrol.* **48**, 589–625.

Stacey J. S. and Kramers J. D. (1975) Approximation of terrestrial lead isotope evolution by a two-stage model. *Earth Planet. Sci. Lett.* **26**, 207–221.

Steiger R. H. and Jäger E. (1977) Subcommission on geochronology: convention on the use of decay constants in geo- and cosmochronology. *Earth Planet. Sci. Lett.* **36**, 359–362.

Sudo A. and Tatsumi Y. (1990) Phlogopite and K-amphibole in the upper mantle: implication for magma genesis in subduction zones. *Geophys. Res. Lett.* **17**, 29–32.

Sweeney R. J., Thompson A. B. and Ulmer P. (1993) Phase relations of a natural MARID composition and implications for MARID genesis, lithospheric melting and mantle metasomatism. *Contrib. Mineral. Petrol.* **115**, 225–241.

Tachibana Y., Kaneoka I., Gaffney A. and Upton B. G. J. (2006) Ocean-island basalt-like source of kimberlite magmas from West Greenland revealed by high $^{3}He/^{4}He$ ratios. *Geology* **34**, 273–276.

Tappe S., Jenner G. A., Foley S. F., Heaman L. M., Besserer D., Kjarsgaard B. A. and Ryan B. (2004) Torngat ultramafic lamprophyres and their relation to the North Atlantic Alkaline Province. *Lithos* **76**, 491–518.

Tappe S., Foley S. F., Jenner G. A. and Kjarsgaard B. A. (2005) Integrating ultramafic lamprophyres into the IUGS classification of igneous rocks: rational and implications. *J. Petrol.* **46**, 1893–1900.

Tappe S., Foley S. F., Jenner G. A., Heaman L. M., Kjarsgaard B. A., Romer R. L., Stracke A., Joyce N. and Hoefs J. (2006) Genesis of ultramafic lamprophyres and carbonatites at Aillik Bay, Labrador: a consequence of incipient lithospheric thinning beneath the North Atlantic craton. *J. Petrol.* **47**, 1261–1315.

Tappe S., Foley S. F., Stracke A., Romer R. L., Kjarsgaard B. A., Heaman L. M. and Joyce N. (2007) Craton reactivation on the Labrador Sea margins: $^{40}Ar/^{39}Ar$ age and Sr–Nd–Hf–Pb isotope constraints from alkaline and carbonatite intrusives. *Earth Planet. Sci. Lett.* **256**, 433–454.

Taylor P. N., Moorbath S., Goodwin R. and Petrykowski A. C. (1980) Crustal contamination as an indicator of the extent of early Archaean continental crust: Pb isotopic evidence from the late Archaean gneisses of West Greenland. *Geochim. Cosmochim. Acta* **44**, 1437–1454.

Thibault Y., Edgar A. D. and Lloyd F. E. (1992) Experimental investigation of melts from a carbonated phlogopite lherzolite: implications for metasomatism in the continental lithospheric mantle. *Am. Miner.* **77**, 784–794.

Tiepolo M., Zanetti A., Oberti R., Brumm R., Foley S. F. and Vannucci R. (2003) Trace-element partitioning between synthetic potassic-richterites and silicate melts, and contrasts with the partitioning behaviour of pargasites and kaersutites. *Eur. J. Mineral.* **15**, 329–340.

Torsvik T. H., Smethurst M. A., Meert J. G., Van der Voo R., McKerrow W. S., Brasier M. D., Sturt B. A. and Walderhaug H. J. (1996) Continental break-up and collision in the Neoproterozoic and Palaeozoic: a tale of Baltica and Laurentia. *Earth Sci. Rev.* **40**, 229–258.

Ulmer P. and Sweeney R. J. (2002) Generation and differentiation of Group II kimberlites: constraints from a high-pressure experimental study to 10 GPa. *Geochim. Cosmochim. Acta* **66**, 2139–2153.

Vervoort J. D. and Blichert-Toft J. (1999) Evolution of the depleted mantle: Hf isotope evidence from juvenile rocks through time. *Geochim. Cosmochim. Acta* **63**, 533–556.

Vervoort J. D., Patchett P. J., Blichert-Toft J. and Albarede F. (1999) Relationships between Lu–Hf and Sm–Nd isotopic systems in the global sedimentary system. *Earth Planet. Sci. Lett.* **168**, 79–99.

Wardle R. J., James D. T., Scott D. J. and Hall J. (2002) The southeastern Churchill Province: synthesis of a Paleoproterozoic transpressional orogen. *Can. J. Earth Sci.* **39**, 639–663.

Waters F. G. (1987) A suggested origin of MARID xenoliths in kimberlites by high pressure crystallization of an ultrapotassic rock such as lamproite. *Contrib. Mineral. Petrol.* **95**, 523–533.

Waters F. G. and Erlank A. J. (1988) Assessment of the vertical extent and distribution of mantle metasomatism below Kimberley, South Africa. *J. Petrol.* **Special Lithosphere Issue**, 185–204.

Waters F. G., Erlank A. J. and Daniels L. R. M. (1989) Contact relationships between MARID rock and metasomatised peridotite in a kimberlite xenolith. *Geochem. J.* **23**, 11–17.

Watson E. B. and Green T. H. (1981) Apatite/ liquid partition coefficients for the rare earth elements and strontium. *Earth Planet. Sci. Lett.* **56**, 405–421.

Wilson M. R., Kjarsgaard B. A. and Taylor B. (2007) Stable isotope composition of magmatic and deuteric carbonate phases in hypabyssal kimberlite, Lac de Gras field, Northwest Territories, Canada. *Chem. Geol.* **242**, 435–454.

Wyllie P. J. (1989) Origin of carbonatites: evidence from phase equilibrium studies. In *Carbonatites: Genesis and Evolution* (ed. K. Bell). Unwin Hyman, London, United Kingdom, pp. 500–545.

Wyllie P. J. and Huang W. L. (1975) Influence of mantle CO_2 in the generation of carbonatites and kimberlites. *Nature* **257**, 297–299.

Associate editor: Martin A. Menzies